

Thermodynamic Properties of the Dipolar Spin Ice Model

Roger G. Melko,^{1,2} Matthew Enjalran,¹ Byron C. den Hertog,¹ and Michel J. P. Gingras^{1,3}

¹*Department of Physics, University of Waterloo, Waterloo, Ontario, N2L 3G1, Canada*

²*Department of Physics, University of California, Santa Barbara, California 93106*

³*Canadian Institute for Advanced Research, 180 Dundas Street West, Toronto, Ontario, M5G 1Z8, Canada*

(Dated: June 1, 2018)

We present a detailed theoretical overview of the thermodynamic properties of the dipolar spin ice model, which has been shown to be an excellent quantitative descriptor of the Ising pyrochlore materials $\text{Dy}_2\text{Ti}_2\text{O}_7$ and $\text{Ho}_2\text{Ti}_2\text{O}_7$. We show that the dipolar spin ice model can reproduce an effective *quasi* macroscopically degenerate ground state and spin-ice behavior of these materials when the long-range nature of dipole-dipole interaction is handled carefully using Ewald summation techniques. This degeneracy is, however, ultimately lifted at low temperature. The long-range ordered state is identified via mean field theory and Monte Carlo simulation techniques. Finally, we investigate the behavior of the dipolar spin ice model in an applied magnetic field, and compare our predictions with experimental results. We find that a number of different long-range ordered states are favored by the model depending on field direction.

I. INTRODUCTION

A. Water Ice and Spin Ice

Frustrated or competing interactions are a common feature of many condensed matter systems.¹ In magnetic materials, frustration arises when the system cannot minimize its total classical ground state energy by minimizing the energy of each spin-spin interaction individually.^{2,3,4} When competing interactions cannot be simultaneously satisfied as a consequence of the arrangement of spins on a geometrical unit, such as a triangle or a tetrahedron, a system made of an assembly of such units is said to be geometrically frustrated. Geometric frustration has been studied extensively in recent years, with the discovery of classical systems that do not display any ordering or dynamical phase transitions down to the lowest temperatures (for recent reviews see Refs. 5-11). Furthermore, much current research effort is being deployed to investigate the exotic behavior of quantum frustrated systems.^{12,13,14,15} In highly frustrated systems, weak quantum fluctuations may work to select a unique ground state that is not stabilized at the classical level, while strong quantum fluctuations (e.g. small spin number value, S) can give rise to novel quantum disordered states.¹⁶ Real material^{17,18,19} and model systems with strongly correlated electrons in the presence of strong magnetic frustration display interesting exotic properties.

While geometric frustration most commonly arises between spins interacting antiferromagnetically (AF), Harris and collaborators^{20,21} showed that the pyrochlore lattice of corner sharing tetrahedra with Ising spins pointing along a local cubic $\langle 111 \rangle$ axis constitutes a new class of geometrical frustration when nearest neighbor interactions are ferromagnetic (FM) (See Fig. 1).^{22,23} As a consequence of the frustration on this lattice, the Ising pyrochlore ferromagnet has a lowest energy ground state configuration that is very closely analogous to an entirely different yet very common frustrated condensed matter

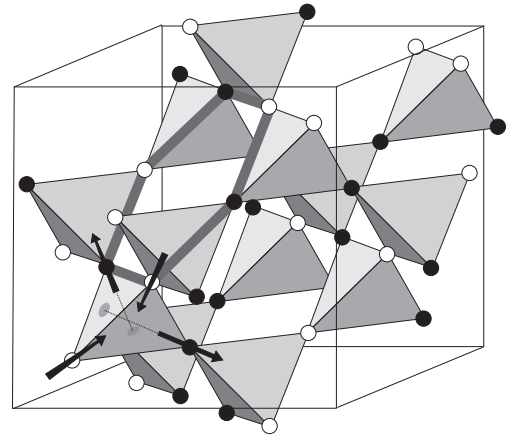


FIG. 1: The $\langle 111 \rangle$ Ising pyrochlore lattice. The lower left “downward” tetrahedron of the pyrochlore lattice shows Ising spins as arrows. Each spin axis is along the local $\langle 111 \rangle$ quantization axis, which goes from one site to the middle of the opposing triangular face (as shown by the disks) and meets with the three other $\langle 111 \rangle$ axes in the middle of the tetrahedron. For clarity, black and white circles on the lattice points denote other spins. White represents a spin pointing into a downward tetrahedron while black is the opposite. The entire lattice is shown in an ice-rules state (two black and two white sites for every tetrahedron). The hexagon (thick gray line) shows a minimal size loop move, which corresponds to reversing all colors (spins) on the loop to produce a new ice-rules state.

system – namely water ice.^{9,11} In the low temperature – low pressure phase of water ice (the so-called “hexagonal ice”, phase I_h), the oxygen atoms are arranged on a hexagonal lattice, each oxygen having four nearest neighbors. Bernal and Fowler²⁴ and Pauling²⁵ were the first to propose that the hydrogen atoms (protons) within the H_2O lattice are not arranged periodically, but are disordered. These hydrogen atoms on the O–O bonds are not

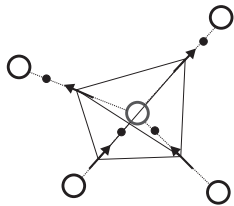


FIG. 2: The local proton arrangement in ice, showing oxygen atoms (large white circles) and hydrogen atoms (small black circles) arranged to obey the ice rules. The displacement of the hydrogen atoms from the mid-points of the oxygen-oxygen bonds are represented as arrows, which translate into spins on the pyrochlore lattice in Fig. 1.

positioned at the mid point between both oxygen atoms, but rather each proton is (covalently) bonded “near” one oxygen and (hydrogen-bonded) “far” from the other such that the water solid consists of hydrogen-bonded H_2O molecules (see Fig. 2). In the Pauling model, ice I_h is established when the whole system is arranged according to the two *ice rules*:

1. Precisely one hydrogen atom is on each proton bond that links two nearest neighbor oxygen atoms.
2. Precisely two hydrogen atoms are near each oxygen atom (spin in) and two are far (spin out) (see Fig. 2).

A consequence of this structure, and the subsequent ice rules, is that there is no single unique lowest energy state. Indeed, there exists an infinitely large number of degenerate low energy states that fulfill the ice rules and, if the degeneracy was truly exact, would manifest itself as a residual entropy at zero temperature (called zero point entropy). Linus Pauling²⁶ estimated theoretically the residual entropy, $S(T \rightarrow 0)$, of ice as

$$S(T \rightarrow 0) \approx \frac{R}{2} \ln \frac{3}{2}, \quad (1)$$

where $R \approx 8.31 \text{ J mole}^{-1}\text{K}^{-1}$ is the molar gas constant. Pauling’s result is not exact, but is accurate to within a few percent compared to experiments.²⁷

Returning to the magnetic Ising pyrochlores, the analogy to water ice arises if the spins are chosen to represent hydrogen displacements from the mid-points of the O–O bonds (Fig. 2). The ice rules of *two protons close, two protons further away* corresponds to the *two spins in – two spins out* configuration of each tetrahedron on the pyrochlore lattice. Because of this direct analogy between water ice and the Ising pyrochlores, Harris *et al.*^{20,21} called the latter *spin ice*.^{9,11,22,23} We note, however, that common water ice at atmospheric pressure, ice I_h , has a hexagonal structure while here, the magnetic lattice has cubic symmetry. Strictly speaking, the Ising pyrochlore problem is equivalent to cubic ice, and not

the hexagonal phase. Yet, this does not modify the “ice-rule” analogy (or mapping) or the connection between the statistical mechanics of the local proton coordination in water ice and the low temperature spin structure of the spin ice materials.

An important point must be emphasized here. In both ice water and spin ice, the microscopic origin of the residual zero point entropy arises from the “simplicity” and “under-constraints” in the problem. Indeed, the constraints (rules) to construct a minimum energy ground state, which arise from the underlying microscopic Hamiltonian, are so “simple” that an infinite number of configurations of the dynamical variables at stake (proton position in ice, and spin direction in spin ice) can be used to make a minimum energy state from which the extensive residual ground state entropy $S(T \rightarrow 0)$ results.

B. Dipolar Spin Ice

Experimentally, it is known that the single ion ground states of the rare earth ions Dy^{3+} and Ho^{3+} in the pyrochlore structure are described by an effective classical Ising doublet.^{20,28} Specific heat measurements by Ramirez²⁹ on the compound $\text{Dy}_2\text{Ti}_2\text{O}_7$ have shown that the “missing” magnetic entropy not recovered upon warming the system from $T \approx 0.4 \text{ K}$ to 10 K , agrees reasonably well with Pauling’s entropy calculation above, $S \approx S(T \rightarrow 0)$, thereby providing compelling thermodynamic evidence that $\text{Dy}_2\text{Ti}_2\text{O}_7$ is a spin ice material³⁰ (see Fig. 3). While early neutron scattering and magnetization measurements first suggested that $\text{Ho}_2\text{Ti}_2\text{O}_7$ was a spin ice material,²⁰ some subsequent specific heat measurements and numerical simulations by Siddharthan and co-workers were interpreted as evidence for a freezing transition to a partially ordered state as opposed to spin ice behavior in that material.^{11,31,32} However, more recent specific heat,^{33,34} magnetization^{34,35} and neutron scattering experiments,³³ supported by Monte Carlo (MC) simulations,³³ appear to confirm the initial proposal²⁰ that $\text{Ho}_2\text{Ti}_2\text{O}_7$ is indeed a spin ice material akin to $\text{Dy}_2\text{Ti}_2\text{O}_7$. Other magnetization measurements have recently been reported that also argue for spin ice behavior in the closely related $\text{Ho}_2\text{Sn}_2\text{O}_7$,^{36,37} $\text{Dy}_2\text{Sn}_2\text{O}_7$,³⁸ and $\text{Ho}_2\text{Ru}_2\text{O}_7$ ³⁹ materials. The dynamical properties of these materials at the spin ice freezing point appear somewhat puzzling and are the subject of an increasing number of studies.^{40,41,42,43}

Following the initial spin ice proposal in 1997 by Harris and co-workers,^{20,21} it appeared that the spin ice materials obeyed the simple ferromagnetic nearest neighbor model mentioned above. This model intuitively gives rise to a degenerate spin ice ground state because of the equivalent energies of the six different tetrahedron configurations that make up the ground state of this geometrically frustrated unit. However, the nearest neighbor spin ice model is too simple to accurately describe the physical

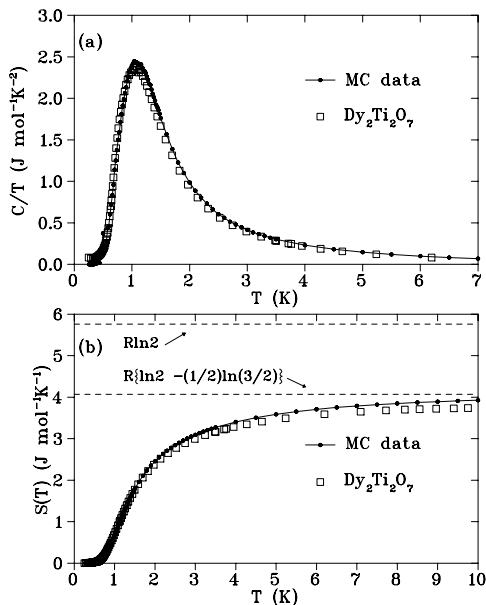


FIG. 3: (a) Specific heat and (b) entropy data for $\text{Dy}_2\text{Ti}_2\text{O}_7$ from Ref. 29, compared with Monte Carlo simulation results for the dipolar spin ice model, with $J_{\text{nn}} = -1.24\text{K}$ and $D_{\text{nn}} = 2.35\text{K}$.

properties of real materials composed of the rare-earth ions Ho^{3+} and Dy^{3+} (see Ref. 31). Firstly, the magnetic cations Ho^{3+} and Dy^{3+} in $\text{Ho}_2\text{Ti}_2\text{O}_7$ and $\text{Dy}_2\text{Ti}_2\text{O}_7$ carry a large magnetic moment,^{20,28} μ , of approximately $10\mu_{\text{B}}$. This entails strong magnetic dipole-dipole interactions in these materials. Indeed, the strength of the dipolar interaction at nearest neighbor distances, D_{nn} , is of order 2 K, which is of the same order of magnitude as the overall magnetic interaction energy scale in these materials as estimated by the Curie-Weiss temperature, $\theta_{\text{CW}} \sim 1$ K, extracted from DC magnetization measurements. Secondly, rare-earth ions possess very small exchange energies, which is roughly the same order of magnitude as θ_{CW} and D_{nn} . Consequently, dipole-dipole interactions in $\text{Ho}_2\text{M}_2\text{O}_7$ and $\text{Dy}_2\text{M}_2\text{O}_7$ ($\text{M}=\text{Ti}, \text{Sn}$) are very significant and constitute an order one energy scale in the problem. This is the reverse of what is observed in transition metal compounds, where the exchange interaction predominates and the dipolar interaction can be treated as a very weak perturbation. Finally, the nearest neighbor exchange interaction in $\text{Ho}_2\text{Ti}_2\text{O}_7$ and $\text{Dy}_2\text{Ti}_2\text{O}_7$ is actually antiferromagnetic, which would by itself cause a phase transition to a Néel long-range ordered $q = 0$ state^{21,23} (see Fig. 5). Consequently, we consider the simplest model of $\langle 111 \rangle$ Ising pyrochlore magnets with both nearest-neighbor exchange and long-range magnetic dipole-dipole interactions with the Hamiltonian:

$$H = -J \sum_{\langle(i,a),(j,b)\rangle} \mathbf{S}_i^a \cdot \mathbf{S}_j^b \quad (2)$$

$$+ D r_{\text{nn}}^3 \sum_{\substack{i > j \\ a, b}} \frac{\mathbf{S}_i^a \cdot \mathbf{S}_j^b}{|\mathbf{R}_{ij}^{ab}|^3} - \frac{3(\mathbf{S}_i^a \cdot \mathbf{R}_{ij}^{ab})(\mathbf{S}_j^b \cdot \mathbf{R}_{ij}^{ab})}{|\mathbf{R}_{ij}^{ab}|^5}.$$

Here the spin vector $\mathbf{S}_i^a = \sigma_i^a \hat{z}^a$ labels the Ising moment of magnitude $|\mathbf{S}_i^a| = 1$ at FCC lattice site \mathbf{R}_i and tetrahedral sub-lattice site coordinate \mathbf{r}^a , where the local Ising axis is denoted by \hat{z}^a and the Ising variable is $\sigma_i^a = \pm 1$. The vector $\mathbf{R}_{ij}^{ab} = \mathbf{R}_{ij} + \mathbf{r}^{ab}$ connects spins \mathbf{S}_i^a and \mathbf{S}_j^b . J represents the exchange energy and D the dipolar energy scale ($J > 0$ and $D = 0$ in the spin ice model originally proposed by Harris *et al.*²¹ which we refer to as the “near neighbor spin ice model”). Because of the relative local $\langle 111 \rangle$ Ising orientations, the nearest neighbor exchange energy between two spins is $J_{\text{nn}} \equiv J/3$. The dipole interaction is calculated from

$$D = \frac{\mu_0}{4\pi} \frac{\mu^2}{r_{\text{nn}}^3}. \quad (3)$$

Experimentally, from magnetization measurements²¹ and analysis of the crystal-field levels via inelastic neutron scattering,²⁸ it is known that the moments of the Dy^{3+} and Ho^{3+} rare-earth ions in the pyrochlore lattice are $\mu \approx 10\mu_{\text{B}}$, and the nearest neighbor distance r_{nn} is approximately 3.54 Angstroms. From Eq. (2), we get the dipole-dipole interaction at nearest neighbor distances to be $D_{\text{nn}} \equiv 5D/3$, since $\hat{z}^a \cdot \hat{z}^b = -1/3$ and $(\hat{z}^a \cdot \mathbf{R}_{ij}^{ab})(\mathbf{R}_{ij}^{ab} \cdot \hat{z}^b) = -2/3$ in Eq. (2). For both $\text{Ho}_2\text{Ti}_2\text{O}_7$ and $\text{Dy}_2\text{Ti}_2\text{O}_7$, $D_{\text{nn}} \approx 2.35\text{K}$.

In order to consider the combined role of exchange and dipole-dipole interactions, it is useful to define an effective nearest neighbor energy scale, J_{eff} , for $\langle 111 \rangle$ Ising spins:

$$J_{\text{eff}} \equiv J_{\text{nn}} + D_{\text{nn}} \quad , \quad (4)$$

where $J_{\text{nn}} \equiv J/3$ is the nearest neighbor exchange energy between $\langle 111 \rangle$ Ising moments. This simple near-neighbor description of the system suggests that a $\langle 111 \rangle$ Ising system could display spin ice properties, even for antiferromagnetic nearest neighbor exchange, $J_{\text{nn}} < 0$, so long as $J_{\text{eff}} = J_{\text{nn}} + D_{\text{nn}} > 0$. Fits to experimental data give $J_{\text{nn}} \sim -0.52$ K for $\text{Ho}_2\text{Ti}_2\text{O}_7$ ³³ and $J_{\text{nn}} \sim -1.24$ K for $\text{Dy}_2\text{Ti}_2\text{O}_7$.⁴⁴ Thus, J_{eff} is positive (using $D_{\text{nn}} = 2.35\text{K}$), hence ferromagnetic and frustrated, for both $\text{Ho}_2\text{Ti}_2\text{O}_7$ ($J_{\text{eff}} \sim 1.8$ K) and $\text{Dy}_2\text{Ti}_2\text{O}_7$ ($J_{\text{eff}} \sim 1.1$ K). It would therefore appear natural to ascribe the spin ice behavior in both $\text{Ho}_2\text{Ti}_2\text{O}_7$ and $\text{Dy}_2\text{Ti}_2\text{O}_7$ to the positive J_{eff} value as in the simple model of Bramwell and Harris.²¹ However, the situation is more complex than it appears.

Dipole-dipole interactions are “complicated”: (i) they are strongly anisotropic since they couple the spin, \mathbf{S}_i^a , and space, \mathbf{R}_{ij}^{ab} , directions, and (ii) they are also very long-ranged ($\propto |\mathbf{R}_{ij}^{ab}|^{-3}$). For example, the second nearest neighbor distance is $\sqrt{3}$ times larger than the nearest neighbor distance, which means that the second nearest neighbor dipolar energy is $D_{\text{nnn}} \sim 0.2D_{\text{nn}}$. This

implies an important perturbation compared to $J_{\text{eff}} = J_{\text{nn}} + D_{\text{nn}} < D_{\text{nn}}$, especially for antiferromagnetic (negative) J_{nn} . Specifically, for $\text{Dy}_2\text{Ti}_2\text{O}_7$, the second nearest neighbor energy scale is about 40% of the effective nearest neighbor energy scale, J_{eff} , a large proportion! Therefore, one might have expected that the dipolar interactions beyond nearest neighbor would cause the different ice-rules states to have different energies, hence possibly breaking the degeneracy of the spin ice manifold, similar to what happens in the kagome⁴⁵ and pyrochlore Heisenberg antiferromagnets⁴⁶ when exchange interactions beyond nearest-neighbor are considered. In Eq. (2), if the dipolar term is summed beyond nearest neighbor, one could expect a long-ranged Néel ordered state at a critical temperature $T_N \sim O(D_{\text{nn}})$. Thus, here arises one of the main puzzling and interesting problems posed by the dipolar spin ice materials that can be summarized by two questions:

1. Are the experimental observations of spin ice behavior in real materials consistent with dominant long-range dipolar interactions?
2. If so, why do long-range dipolar interactions fail to destroy spin ice behavior and give rise to long-range order at a temperature $T_N \sim O(D_{\text{nn}})$?

Results from Monte Carlo simulations on the dipolar spin ice model attempting to answer the first question above were first reported in Ref. 31 and Ref. 32. In that work, the dipole-dipole interactions were cut-off at a distance of five³¹ or ten and twelve nearest-neighbors.³² In those studies the thermodynamic behavior was found to be consistent with spin ice behavior for a model of $\text{Dy}_2\text{Ti}_2\text{O}_7$, provided the exchange interaction was made to extend far beyond nearest neighbor,⁴⁷ but not for a model of $\text{Ho}_2\text{Ti}_2\text{O}_7$. A subsequent work,⁴⁴ considered the Hamiltonian of Eq. (2) with only nearest-neighbor exchange and the value of J as an adjustable parameter. In that work, the long-range dipole-dipole interaction was handled using the well-known Ewald method, which derives an effective dipole-dipole interaction between spins within the cubic simulation cell. The Monte Carlo simulations were carried out by slowly cooling the simulated lattice, subject to the usual Metropolis algorithm. Numerical integration of the specific heat divided by temperature was performed to determine the entropy of the system.⁴⁴ For a parameter J appropriate for the $\text{Dy}_2\text{Ti}_2\text{O}_7$ spin ice material (see Section II below), the dipolar spin ice model retained Pauling's entropy (Eq. (1)), in good agreement with experiments on $\text{Dy}_2\text{Ti}_2\text{O}_7$ (Fig. 3). Following the same approach as in Ref. 44, recent Monte Carlo simulations have found good agreement between the dipolar spin ice model, specific heat measurements and elastic neutron scattering, as well as experiments on $\text{Ho}_2\text{Ti}_2\text{O}_7$.³³ Finally, mean-field theory calculations of the neutron scattering intensity, valid in the (paramagnetic) temperature regime $T \gg \theta_{\text{CW}}$ that consider large distance cut-off of the dipole-dipole interactions have been found to be in good agreement with

experiments on $\text{Ho}_2\text{Sn}_2\text{O}_7$ ³⁷ and $\text{Ho}_2\text{Ti}_2\text{O}_7$.⁴⁸ Consequently, there is now strong compelling evidence that the long-range dipolar interaction is responsible for the ice behavior and the subsequent retention of zero-point entropy in rare-earth based insulating pyrochlore magnets.⁹

C. True Long Range Order at Low Temperature in the Dipolar Spin Ice Model

Having answered question #1 above in the affirmative, one is then faced with addressing question #2. The Monte Carlo results mentioned above⁴⁴ show that spin ice behavior arises from the combination of nearest-neighbor exchange, J_{nn} , and dipole energies, D_{nn} , which create an *effective* ferromagnetic Ising model J_{eff} at nearest neighbor as long as $J_{\text{eff}} \equiv J_{\text{nn}} + D_{\text{nn}} \gtrsim 0$, akin to Harris and Bramwell's simple nearest-neighbor Ising model.^{20,21,49,50} However, the long-range dipolar interaction does not appear to destroy the spin ice degeneracy (and subsequent retention of zero point entropy) created by this effective ferromagnetic nearest neighbor interaction. In support of this picture, a mean-field theory (MFT) calculation finds that remaining (beyond nearest neighbor) dipole-dipole interaction terms, which couple every spin in the system with varying strength depending on their separation distance, is "screened" to a large degree.^{51,52} This means that the degeneracy between different ice-rules obeying states is almost exactly fulfilled by carefully including the long distance dependence of the dipolar term in the Hamiltonian. However, and perhaps most interestingly for these Ising pyrochlore systems, the same mean-field calculation suggests that the screening of the long-range terms is not perfect, and that the associated spin ice manifold is only *quasi*-degenerate, due to some small remaining effective energy scale, and that a unique ordering wavevector is selected.^{48,51,52} This suggests that at some temperature below the onset temperature of spin ice correlations, the dipolar spin ice model should in principle favor the unique long-range ordered state selected by this remaining ("unscreened") perturbative dipole-dipole energy.

One might naively expect that such an ordered state should be found in the MC simulations.^{33,44,53} However, this does not happen, as measurements of the temperature dependent acceptance rate of the simulations make it apparent that the standard single (Ising) spin flip Metropolis algorithm experiences a dynamical "freezing" at a temperature ≈ 0.3 K for J_{nn} and D_{nn} parameters appropriate for $\text{Dy}_2\text{Ti}_2\text{O}_7$ ⁴⁴ and $T \approx 0.6$ K for $\text{Ho}_2\text{Ti}_2\text{O}_7$.³³ If the dipolar interactions are cut-off at some arbitrary distance, R_c , one can generate scenarios where, depending on specific numerical values for J_{nn} , D_{nn} and R_c , a selected state is dynamically accessible before the spin-ice manifold freeze-out, as was found in simulations where dipole interactions are cut-off.^{31,32} Consequently, akin to the approaches used in ice lattice models,^{56,57} one must introduce non-local dynamics in the simulation to com-

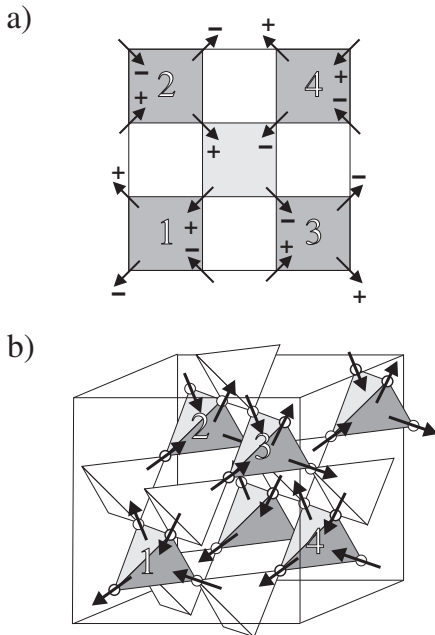


FIG. 4: The long-range ordered $\mathbf{q} = (0, 0, 2\pi/a)$ dipolar spin ice ground state. Projected down the z axis (a), the four tetrahedra making up the cubic unit cell appear as dark gray squares. The light gray square in the middle does not represent a tetrahedron, but its diagonally opposing spins are in the same lattice plane. The component of each spin parallel to the z axis is indicated by a + and - sign. In perspective (b), the four tetrahedra of the unit cell are numbered to enable comparison with (a).

but this freezing-out and maintain simulation equilibrium down to lower temperatures. The inclusion of non-local “loop moves” in the dipolar spin ice model promotes the development of a long-range ordered phase via a sharp first order phase transition at $T \approx 0.18$ K,^{58,59} a much lower temperature than the onset temperature for spin ice correlations at $T \sim 1.2$ K in $\text{Dy}_2\text{Ti}_2\text{O}_7$ ^{29,44} and $T \sim 1.9$ K in $\text{Ho}_2\text{Ti}_2\text{O}_7$.³³ The ground state found in the loop MC simulations has zero total (bulk) magnetization (recall that each tetrahedron individually carries a net magnetic moment in each of the ice-rule obeying states). See Fig. 4 for the spin configurations in this ground state. The pre-transitional specific heat and the latent heat associated with the first order transition recovers all of Pauling’s missing entropy in the model. The ordered state that is found in the loop MC simulations⁵⁸ corresponds to the ordered state predicted by mean field theory.^{51,52} In other words, the dipolar spin ice model possesses on its own, without invoking energetic perturbations and/or thermal and quantum fluctuations, a unique (up to trivial global symmetry relations) classical ground state with zero extensive entropy.

Also, using MC simulations and direct Ewald energy calculations, we investigate the behavior of the dipolar

spin ice model in an external magnetic field. With application of a large field along three different crystal symmetry directions, three different long-range ordered ground states appear. With large fields parallel to the $[100]$ crystal direction, the ground state is the ice-rules $\mathbf{q} = 0$ structure identified by Harris.²⁰ For large fields parallel to $[110]$, the ground state is the ice-rules $\mathbf{q} = X$ state,²⁰ and for large fields along $[111]$, the ice rules are broken and a three-spin in, one-spin out spin configuration becomes the lowest energy state. The experimentally determined field dependence of the magnetization and specific heat for fields along the $[100]$, $[110]$ and $[111]$ directions in the $\text{Dy}_2\text{Ti}_2\text{O}_7$ spin ice material agree quantitatively well with the Monte Carlo results for the long-range dipolar spin ice model.^{60,61,62,63,64}

D. Phases of Dipolar Spin Ice

Using Monte Carlo simulations, the phase diagram for the dipolar spin ice model can be mapped out (Fig. 5). To summarize the results, spin ice correlations develop for all cases where the effective nearest neighbor energy scale $J_{\text{eff}}/D_{\text{nn}} > 0.095$ (ferromagnetic), and the temperature is below the broad peak in the specific heat, T_{peak} . For $T/D_{\text{nn}} \leq 0.08$, independent of the value of J_{nn} (as long as $J_{\text{eff}}/D_{\text{nn}} > 0.095$), the system orders into the long-range ordered state, with the help of the loop moves in the simulation. For $J_{\text{nn}}/D_{\text{nn}}$ less than -0.905 ($J_{\text{eff}}/D_{\text{nn}} < 0.095$), the system orders into an antiferromagnetic $\mathbf{q} = 0$ Néel ground state, where every tetrahedron in the system has an all-in or all-out spin configuration at low temperatures.^{21,23,65,66} The region around $J_{\text{nn}}/D_{\text{nn}} = -1$ shows hysteresis at low temperatures. Because of the close cancellation of energy scales, we imagine that real materials which fall into this region, e.g., $\text{Tb}_2\text{Ti}_2\text{O}_7$,^{67,68,69,70} will be particularly susceptible to the influence of small perturbations (such as exchange beyond nearest-neighbor or finite, as opposed to infinite, Ising anisotropy^{52,71}) with the result of possible ordering into long-range ordered states⁷² distinct from the two shown in Fig. 5.

E. Outline

The rest of the paper is organized as follows. In the next section we present results from conventional single spin flip Monte Carlo simulations that show how spin ice behavior develops at finite temperatures in the dipolar spin ice system whenever the effective nearest-neighbor coupling is ferromagnetic ($J_{\text{eff}} \equiv J_{\text{nn}} + D_{\text{nn}} \gtrsim 0$). Results from mean-field theory are presented in Section III. There we show that there exists a weak selection of a unique ordering (critical or soft mode) at $\mathbf{q} = (0, 0, 2\pi/a)$. Motivated by our mean-field results, we undertake a numerical search for a long-range ordered state in the model of Eq. (2). Section IV discusses the details of a loop Monte

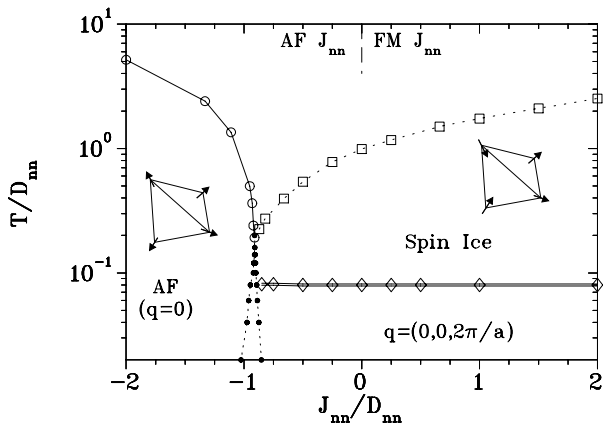


FIG. 5: The phase diagram for the dipolar spin ice model. The antiferromagnetic ground state is an all-spins-in or all-spins-out configuration for each tetrahedron. The spin ice configuration, which includes the $\mathbf{q} = (0, 0, 2\pi/a)$ ground state, is a two spins in-two spins out configuration for each tetrahedron. The region encompassed between the quasi vertical dotted lines displays hysteresis in the long-range ordered state selected ($\mathbf{q} = 0$ vs. $\mathbf{q} = (0, 0, 2\pi/a)$) as J_{nn}/D_{nn} is varied at fixed temperature T .

Carlo algorithm that avoids the freezing phenomenon observed in a MC simulation employing local single spin flip dynamics. Section V presents the detailed results from the loop Monte Carlo simulations. The results for the field dependence of the ground state energy and magnetization for fields along [100], [110] and [111] are presented in Section VI. We conclude the paper with a brief discussion in Section VII. We have included several appendixes. Appendix A contains a discussion of the Ewald technique for dipolar interactions in real space (MC simulations) and in momentum space (MFT). In Appendix B, the \mathbf{q} -dependent susceptibility, to quadratic order, is derived via high temperature series expansion to demonstrate the connection of the mean-field T_c to the onset of long-range correlations. Appendix C discusses some of the effects of a finite demagnetization factor on specific heat results.

II. THE DIPOLAR SPIN ICE MODEL: CONVENTIONAL METROPOLIS MONTE CARLO

In this Section we present the results of Monte Carlo simulations of the dipolar spin ice Hamiltonian 2 using a standard single spin flip Metropolis algorithm. To use Eq. (2) within a simulation, the dipole-dipole interaction must be handled with care. A lattice summation of such interactions is conditionally convergent due to its $1/R^3$ nature. In order to properly handle the long-range nature of this term, we implement the well known Ewald method in the simulations, which derives an effective dipole-dipole interaction between spins within the

simulation cell.⁷³ Unlike in dipolar fluid simulations,⁷⁴ the pyrochlore lattice constrains the positions of the spins in the simulation, allowing the Ewald interactions to be calculated only once, after which a numerical simulation can proceed as normal. Appendix A contains a brief discussion of the Ewald method applied to MC real space simulations.

Simulations on the dipolar spin ice model are carried out using the standard single spin flip Metropolis algorithm. To mimic the experimental conditions pertinent to real materials, the simulation sample is cooled slowly. At each temperature step, the system is equilibrated carefully, then thermodynamic quantities of interest are calculated. Since D_{nn} can be determined once the crystal field structure of the magnetic ion is known, the nearest neighbor exchange J_{nn} is the only adjustable parameter in the model. The single spin flip Metropolis algorithm is able to map out three different regions of the phase diagram shown in Fig. 5. Thermodynamic data indicates that when the nearest neighbor exchange is AF and sufficiently large compared to the dipolar interactions ($J_{nn} < 0$ and $|J_{nn}| \gg D_{nn}$), the system undergoes a second order phase transition (in the three dimensional Ising universality class) to an all-in or all-out $\mathbf{q} = 0$ ground state. In the spin ice regime, $J_{\text{eff}} = J_{nn} + D_{nn} \gtrsim 0$, each specific heat data set for different J_{nn} shows qualitatively the same broad peak as observed in the nearest neighbor FM exchange model,⁴⁹ which vanishes at high and low temperatures (see Fig. 6). The height, C_{peak} ,

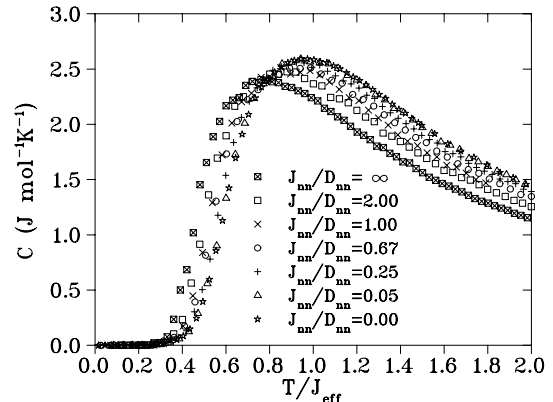


FIG. 6: Specific heat for system size $L = 2$, with temperature, T , re-scaled into units of the effective nearest neighbor interaction $J_{\text{eff}} \equiv J_{nn} + D_{nn}$. $J_{nn}/D_{nn} = 0$ corresponds to purely dipolar interactions, while $J_{nn}/D_{nn} = \infty$ corresponds to nearest neighbor FM exchange only. Simulation runs for $L = 4$ were also performed, but revealed no important finite size effects.

and peak temperature position of this peak, T_{peak} , show very little dependence on system size, for simulation cells of $L = 2, 3, 4, 5$ and 6. However, both C_{peak} and T_{peak} are found to depend strongly on the ratio of J_{nn}/D_{nn} , as illustrated in Fig. 7.

By re-scaling the temperature scale for the specific heat

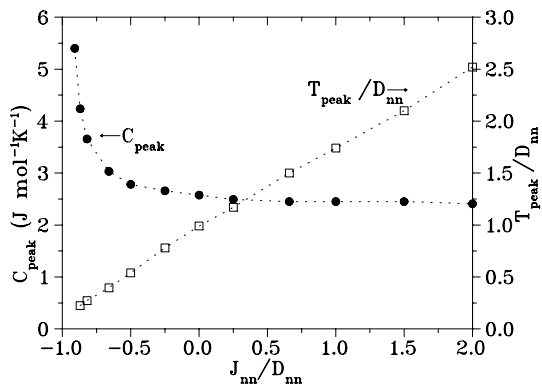


FIG. 7: Dependence of the simulated specific heat peak height C_{peak} and temperature location of C_{peak} and T_{peak} on exchange and dipole-dipole interaction parameters. In this figure D_{nn} is set to 2.35K.

corresponding to a number of different interaction parameters J_{nn} and D_{nn} , one can expose more clearly the dependence of the specific heat on the competition between the nearest neighbor exchange J_{nn} and the dipole-dipole interactions. In Fig. 6, this dependence is illustrated in the regime $J_{\text{nn}}/D_{\text{nn}} > 0$. This figure shows that in terms of an effective energy scale, J_{eff} , the medium to long-range effects of the dipolar interactions are in some sense “screened” by the system, and one recovers qualitatively the short range physics of the nearest neighbor spin ice model. As the nearest neighbor exchange interaction becomes AF (see Fig. 7 for $J_{\text{nn}}/D_{\text{nn}} < 0$), we find that the approximate collapse onto a single energy scale becomes less accurate, with the specific heat becoming dependent on $J_{\text{nn}}/D_{\text{nn}}$. It is within this regime that we believe that both $\text{Ho}_2\text{Ti}_2\text{O}_7$ and $\text{Dy}_2\text{Ti}_2\text{O}_7$ are realized, as we now discuss.

Since D_{nn} is calculated from Eq. (3), J_{nn} must be determined from experimental data. By fitting either the height C_{peak} or the peak temperature T_{peak} of the maximum of the specific heat curves of the Monte Carlo simulation to the experimental results²⁹ (Fig. 3a), we obtain a value of $J_{\text{nn}} = -1.24\text{K}$ for $\text{Dy}_2\text{Ti}_2\text{O}_7$. The results of this fitting are illustrated in the top panel of Fig. 3. A fitting of the height or peak temperature of the experimental magnetic contribution to specific heat for $\text{Ho}_2\text{Ti}_2\text{O}_7$ gives $J_{\text{nn}} = -0.52\text{K}$ for this material.³³ Contrary to what is reported in Ref. 32, we, therefore, conclude that $\text{Ho}_2\text{Ti}_2\text{O}_7$ is “deeper” (J_{eff} more positive for $\text{Ho}_2\text{Ti}_2\text{O}_7$ than for $\text{Dy}_2\text{Ti}_2\text{O}_7$) in the spin ice regime (farther to the right in Fig. 5) than $\text{Dy}_2\text{Ti}_2\text{O}_7$. As initially reported in Ref. 75, the temperature dependence of the specific heat for $\text{Ho}_2\text{Ti}_2\text{O}_7$, is less straightforward to interpret than for $\text{Dy}_2\text{Ti}_2\text{O}_7$.²⁹ In $\text{Ho}_2\text{Ti}_2\text{O}_7$ the specific heat possesses an important contribution from a nuclear component due to a large hyperfine splitting of the nuclear levels well known to occur for Ho^{3+} cations, as discussed in Ref. 76 and Ref. 77. This nuclear component was estimated by Blöte *et al.*⁷⁶ for $\text{Ho}_2\text{GaSbO}_7$. By

subtracting it off from the (total) experimental specific heat, we can uncover the underlying magnetic contribution and compare to the theoretically calculated Monte Carlo specific heat data, from which T_{peak} or C_{peak} can be determined directly (Fig. 8). We note here, as recently observed in Ref. 78, that for $\text{Dy}_2\text{Ti}_2\text{O}_7$ there should be a hyperfine nuclear contribution to the specific heat manifesting itself at a temperature below $T \lesssim 0.4\text{K}$ in the data of Ref. 29 if one uses the typical hyperfine contact interaction expected for a Dy^{3+} insulating salt. The absence of the high temperature $1/T^2$ tail of the nuclear specific heat (on the descending low temperature side of the magnetic specific heat of $\text{Dy}_2\text{Ti}_2\text{O}_7$) below 0.4 K in Fig. 3a is, therefore, somewhat puzzling.⁷⁹

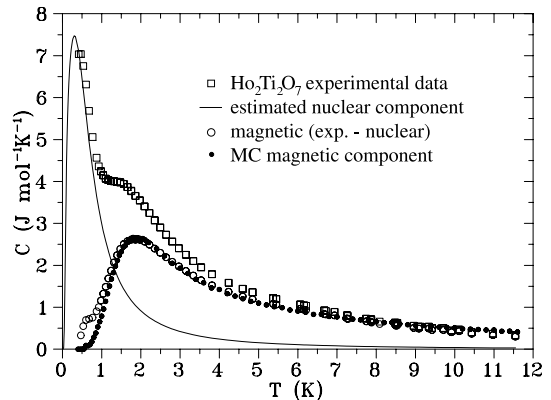


FIG. 8: The total experimental specific heat of $\text{Ho}_2\text{Ti}_2\text{O}_7$ is shown by the open squares. The expected nuclear contribution is indicated by the line, while the resulting magnetic specific heat estimation is shown by the open circles. Near 0.7 K the estimation is prone to a large error. Dipolar spin ice simulation results are indicated by the filled circles.

The shoulder-like feature in the estimated magnetic contribution to the experimental specific heat data of Fig. 8 (open circles) near 0.7 K can be entirely eliminated by adjusting the nuclear hyperfine splitting by $\sim 2\%$ percent around the value estimated by Blöte for $\text{Ho}_2\text{GaSbO}_7$, resulting in an exceedingly good agreement with the Monte Carlo results down to $T = 0.4\text{K}$. Such a slight adjustment to account for any small deviations in the hyperfine parameters of $4f$ rare-earth ions (dependent upon electric field gradients, chemical shift, etc.) would seem reasonable. However, we do not do this in order to emphasize that the unbiased use of the estimated nuclear specific heat contribution from the isostructural material $\text{Ho}_2\text{GaSbO}_7$ ⁷⁶ already allows for a very good agreement with the theoretical magnetic specific heat.

Having determined J_{nn} and D_{nn} for $\text{Ho}_2\text{Ti}_2\text{O}_7$ from specific heat measurements, we are able to compare the experimental elastic neutron scattering against that determined via the Monte Carlo simulations. The results, reported in Ref. 33, show excellent agreement between experiment and simulation. More recent neutron scattering experiments on the $\text{Ho}_2\text{Sn}_2\text{O}_7$ show similar results.³⁷

Such comparison between theory and experiments for $\text{Dy}_2\text{Ti}_2\text{O}_7$ is more difficult due to the large neutron absorption cross section of naturally occurring Dy isotopes. Work in that direction using isotopically enriched samples with ^{162}Dy isotope is in progress.⁸⁰

Numerical integration of the specific heat divided by temperature can be performed to determine the entropy of both $\text{Ho}_2\text{Ti}_2\text{O}_7$ and $\text{Dy}_2\text{Ti}_2\text{O}_7$. Specifically, the entropy, $S(T)$, removed between temperature T_1 and T_2 , $S(T_2) - S(T_1)$, can be calculated using the thermodynamic relation:

$$S(T_2) - S(T_1) = \int_{T_1}^{T_2} \frac{C(T)}{T} dT. \quad (5)$$

The results for $\text{Dy}_2\text{Ti}_2\text{O}_7$ are illustrated in Fig. 3b. The entropy recovered between $T = 0.4\text{K}$, where $C(T)$ is very small, up to a temperature $T = 10\text{K}$, is $S(T = 10\text{K}) - S(T \approx 0) \approx 3.930 \text{ J mol}^{-1} \text{ K}^{-1}$. As we can see in Fig. 3b, the Monte Carlo data for $S(T)$ at $T = 10 \text{ K}$ is slightly below the Pauling's value $R\{\ln(2) - (1/2)\ln(3/2)\}$. To perform the calculation of the recovered entropy between $T = 10 \text{ K}$ up to $T = \infty$, we extrapolate the temperature specific heat $C(T)$ for $T > 10 \text{ K}$ by matching the Monte Carlo value of $C(T)$ at $T = 10 \text{ K}$ with the $1/T^2$ high temperature paramagnetic temperature regime, $C(T) = C_\infty/T^2$ for $T > 10\text{K}$. This gives a value $C_\infty = 29.015 \text{ J mol}^{-1} \text{ K}$, and an extra entropy of $S(T = \infty) - S(T = 10) = 0.145 \text{ J mol}^{-1} \text{ K}^{-1}$, hence a value $S(T = \infty) - S(T \approx 0) = 4.075 \text{ J mol}^{-1} \text{ K}^{-1}$, in exceedingly close agreement with Pauling's value, $4.077 \text{ J mol}^{-1} \text{ K}^{-1}$. Hence, we find that the simulation with the appropriate experimental parameters retains Pauling's entropy (Eq. (1)), similar to what is found experimentally for $\text{Dy}_2\text{Ti}_2\text{O}_7$ (Fig. 3b and in Ref. 29). A similar experimental procedure was done using the magnetic contribution of the specific heat data of $\text{Ho}_2\text{Ti}_2\text{O}_7$, also giving a residual entropy close to Pauling's entropy.³⁴

While the above conventional Monte Carlo simulations of the model Hamiltonian for the spin ice compounds, Eq. (2), yields a reasonably successful quantitative theory of spin ice behavior in Ising pyrochlore materials, there still remains the second question (# 2, Section IB) as to why dipolar interactions, despite their anisotropic and long-range nature, do not (appear to) lift the macroscopic degeneracy associated with the ice rules, and select an ordered state. As a first attempt to address this, we investigate the spectrum of soft modes (i.e. critical modes or ordering wave vectors) accessible to the dipolar spin ice model within the context of mean-field theory.

III. MEAN FIELD THEORY

In this section we present the main results of a mean-field theory calculation aimed at determining the spectrum of soft modes in the dipolar spin ice model. The details of the method can be found elsewhere.^{46,52,81}

The MC simulation results presented in the previous section answer in the affirmative the question as to whether or not long-range dipole-dipole interactions in real materials are consistent with the manifestation of spin ice behavior in a temperature range $0 < T < \theta_{\text{CW}}$. However, these results do not address the question of whether or not a true ground state degeneracy and failure to order at any nonzero temperature is an exact symmetry consequence of the long-range dipolar interactions for $\langle 111 \rangle$ Ising spins on the pyrochlore lattice. A direct way to address this question is to ask whether or not there actually exists at the Gaussian level (i.e. MFT) a soft or critical mode in the model at a well-defined ordering wave vector \mathbf{q} . The results of this calculation for finite distance cut-off, R_c , of the dipole-dipole interactions have been reported in a conference proceedings.⁵¹ We briefly review the essence of the calculation and extend it to untruncated (true long-range $1/R^3$) dipole-dipole interactions using the Ewald summation technique. In MFT the Ewald technique is implemented in \mathbf{q} -space, in contrast to real space for MC simulations. The approach is briefly discussed in Appendix A.

Our MF derivation begins with the Hamiltonian for $\langle 111 \rangle$ Ising spins, Eq. (2), but expressed in terms of the Ising variables, σ_i^a , and local quantization axes, \hat{z}^a ,

$$H = -\frac{1}{2} \sum_{i,j} \sum_{a,b} \mathcal{J}^{ab}(i,j) \sigma_i^a \sigma_j^b, \quad (6)$$

where

$$\begin{aligned} \mathcal{J}^{ab}(i,j) = & J(\hat{z}^a \cdot \hat{z}^b) \delta_{\mathbf{R}_{ij}^{ab}, \mathbf{R}_{nn}} \\ & - D_{dd} \left(\frac{\hat{z}^a \cdot \hat{z}^b}{|\mathbf{R}_{ij}^{ab}|^3} - \frac{3(\hat{z}^a \cdot \mathbf{R}_{ij}^{ab})(\hat{z}^b \cdot \mathbf{R}_{ij}^{ab})}{|\mathbf{R}_{ij}^{ab}|^5} \right). \end{aligned} \quad (7)$$

Recall that indices a and b denote the sub-lattice and \mathbf{R}_{ij}^{ab} is the vector that connects spins σ_i^a and σ_j^b . The pyrochlore lattice is a non-Bravais lattice which is described in a rhombohedral basis with four atoms per unit cell located at positions \mathbf{r}^a given by $(0, 0, 0)$, $(1/4, 1/4, 0)$, $(1/4, 0, 1/4)$, and $(0, 1/4, 1/4)$ in units of the conventional cubic unit cell of size $a = R_{\text{nn}}\sqrt{8}$. Each of these four points define a fcc sub-lattice of cubic unit cell size a . Using H from Eq. (6), we form the free energy of our system,

$$F = \text{Tr}\{\rho H\} + T\text{Tr}\{\rho \ln \rho\}, \quad (8)$$

where ρ is the many-body density matrix.

The first step in the mean-field approximation entails replacing ρ with the product of single-particle density matrices ($\rho(\{\sigma_i^a\}) = \prod_{i,a} \rho_i^a(\sigma_i^a)$). Next, a variational free energy is obtained by treating the $\rho_i^a(\sigma_i^a)$ as variational parameters subject to the constraints $\text{Tr}\{\rho_i^a\} = 1$ and $\text{Tr}\{\rho_i^a \sigma_i^a\} = m_i^a$, where m_i^a is the local magnetization, or order parameter. The resulting variational free energy is transformed to momentum space. Our convention for the Fourier transform employs the position of the

local magnetization, \mathbf{R}_i^a ,

$$m_i^a = \sum_{\mathbf{q}} m_{\mathbf{q}}^a e^{-i\mathbf{q}\cdot\mathbf{R}_i^a}, \quad (9)$$

from which the spin interaction matrix can be expressed in terms of its Fourier components,

$$\mathcal{J}^{ab}(i, j) = \frac{1}{N_{\text{cell}}} \sum_{\mathbf{q}} \mathcal{J}^{ab}(\mathbf{q}) e^{i\mathbf{q}\cdot\mathbf{R}_{ij}^{ab}}, \quad (10)$$

where N_{cell} is the number of four atom unit cells, i.e., fcc lattice points. We note that the above convention for the Fourier transform produces a symmetric 4×4 matrix $\mathcal{J}(\mathbf{q})$ at all values of \mathbf{q} . An alternate convention defining the Fourier transform with respect to the Bravais lattice points, \mathbf{R}_i , results in a complex (Hermitian) $\mathcal{J}(\mathbf{q})$, as discussed in Ref. 52. From Eqs. (9) and (10), we write the quadratic part of the MF free energy, $F^{(2)}$,

$$f^{(2)}(T) = \frac{1}{2} \sum_{\mathbf{q}} \sum_{a,b} m_{\mathbf{q}}^a \{T\delta^{ab} - \mathcal{J}^{ab}(\mathbf{q})\} m_{-\mathbf{q}}^b, \quad (11)$$

where $f^{(2)}(T) = F^{(2)}(T)/N_{\text{cell}}$ and T is the temperature in units of $1/k_B$. Diagonalizing $f^{(2)}(T)$ requires transforming to the normal modes of the system,

$$m_{\mathbf{q}}^a = \sum_{\alpha=1}^4 U^{a,\alpha}(\mathbf{q}) \Phi_{\mathbf{q}}^{\alpha}, \quad (12)$$

where the Greek index α labels normal modes, $\{\Phi_{\mathbf{q}}^{\alpha}\}$ are the amplitudes of the normal modes, and $U(\mathbf{q})$ is the unitary matrix that diagonalizes $\mathcal{J}(\mathbf{q})$ in the sub-lattice space, with eigenvalues $\lambda(\mathbf{q})$,

$$U^{\dagger}(\mathbf{q})\mathcal{J}(\mathbf{q})U(\mathbf{q}) = \lambda(\mathbf{q}). \quad (13)$$

In component form, $U^{a,\alpha}(\mathbf{q})$ represents the a -component of the α -eigenvector. We express $f^{(2)}(T)$ in terms of normal modes as

$$f^{(2)}(T) = \frac{1}{2} \sum_{\mathbf{q}} \sum_{\alpha} \Phi_{\mathbf{q}}^{\alpha} \{T - \lambda^{\alpha}(\mathbf{q})\} \Phi_{-\mathbf{q}}^{\alpha}. \quad (14)$$

In our approach, a minus sign was pulled out in front of the Hamiltonian in Eq. 6, therefore, an ordered state first occurs at the temperature defined by the global maximum eigenvalue,

$$T_c = \max_{\mathbf{q}} \{\lambda^{\max}(\mathbf{q})\}, \quad (15)$$

where $\lambda^{\max}(\mathbf{q})$ is the largest of the four eigenvalues ($\alpha = 1, 2, 3, 4$) at wave vector \mathbf{q} , and $\max_{\mathbf{q}}$ indicates the global maximum of the spectrum of $\lambda^{\max}(\mathbf{q})$ for all \mathbf{q} . The value of \mathbf{q} for which $\lambda^{\max}(\mathbf{q})$ is maximum is the ordering wavevector \mathbf{q}_{ord} .

In Ref. 51, we evaluated $\mathcal{J}(\mathbf{q})$ in the spin ice regime of our model ($J_{\text{nn}}/D_{\text{nn}} = 0$) directly from the inverse

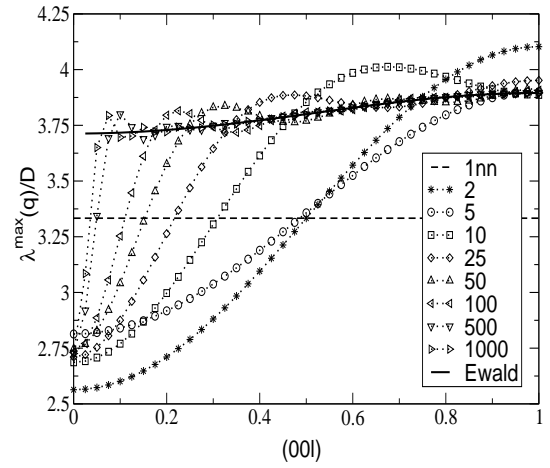


FIG. 9: $\lambda^{\max}(\mathbf{q})/D$ vs. \mathbf{q} for \mathbf{q} in the $(00l)$ direction, in units of $2\pi/a$, for various cut-off distances, R_c , and for the infinite range limit simulated by the Ewald summation technique. Calculations were made at $J_{\text{nn}}/D_{\text{nn}} = 0$ on the spin ice side of the phase diagram, Fig. 5.

transform of Eq. (10) for various real-space cut-off distances of the dipolar term. For the rather dramatic approximation of nearest-neighbor distances, we found a complete degeneracy (\mathbf{q} -independence) of λ^{\max} over the whole Brillouin zone. This corresponds to the \mathbf{q} -space signature of the degenerate nearest-neighbor spin ice model of Harris and Bramwell,²¹ and, equivalently, of the nearest-neighbor (global) Ising antiferromagnet model of Anderson.²² As R_c was increased, a R_c -dependent \mathbf{q}_{ord} appeared. In the limit of infinite range interactions, i.e., $R_c \rightarrow \infty$, we predicted $\mathbf{q}_{\text{ord}} = (001)$ (in units of $2\pi/a$). Results for λ^{\max} along the $(00l)$ direction as a function of R_c are shown in Fig. 9.

Treating dipolar interactions via the Ewald method, where the true long-range nature of the interactions are respected, we observe a completely smooth (without ripples) and quasi-degenerate soft mode spectrum with a global maximum (critical mode) at (001) . The spectrum of $\lambda^{\max}(\mathbf{q})/D$ in the (hhl) plane of the pyrochlore lattice for $J_{\text{nn}} = 0$ is shown in Fig. 10, while the results along the $(00l)$ direction are included in Fig. 9. Inspection of corresponding eigenvectors of the doubly degenerate critical mode indicate a two-in two-out spin ice structure, where the spins on sub-lattices $a = 1, 3$ point opposite to those on sub-lattices $a = 2, 4$ in a tetrahedral unit, see Table I. Ref. 52 discusses how these soft modes can be used to reconstruct the long-ranged ordered (equal moment) structure, where the thermal local magnetization is the same on all sites, and which corresponds to the long-range ordered two-in two-out spin ice state of Fig. 4.

With the implementation of the Ewald method, we are able to study the symmetry properties of the long-range dipolar interactions in a controlled manner. This is a desirable feature for a problem like spin ice because dipole-dipole interactions beyond nearest neighbor distances in-

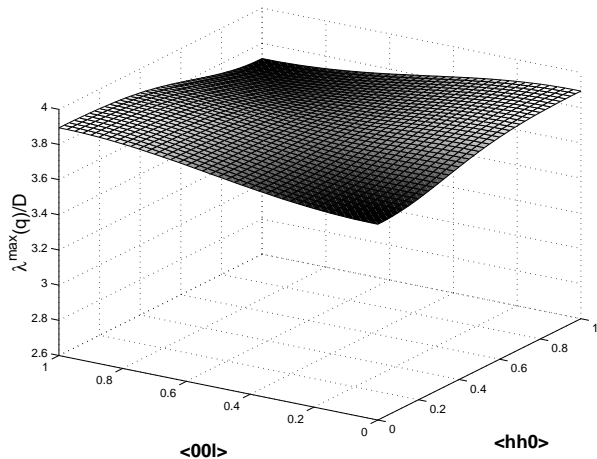


FIG. 10: The scaled maximum eigenvalues, $\lambda^{\max}(\mathbf{q})/D$, in the (hhl) plane for the same spin ice model described in Fig. 9. The dipole-dipole interactions are treated with the Ewald approach.

roduce perturbations onto the highly degenerate soft mode spectrum of the parent state, the nearest neighbor spin ice model. The form of the dipolar interaction, which couples spin and spatial degrees of freedom, permits both positive and negative contributions to the total dipolar energy as R_c is increased, so the interactions are self-screening. However, this symmetry is not exact and the value for \mathbf{q}_{ord} in MFT depends crucially but unpredictably on how far the sum is carried out. The variability in \mathbf{q}_{ord} is readily observed for short cut-off distances, e.g., $R_c \lesssim 100\text{nn}$. However, subtle effects are still present even at very large cut-off distances and can produce an anomalous ordering wave vector. With the dipolar interactions cut-off at $R_c = 1000\text{nn}$, an incommensurate critical mode is found at $\mathbf{q} \sim (0.025, 0.025, 1.0)$. This mode is singly degenerate (unlike the doubly degenerate mode at (001) in the Ewald limit) and the eigenvectors do not predict a two-in two-out spin ice structure. We underscore, again, that this effect is subtle, as is demonstrated by the difference in the eigenvalues at $R_c = 1000\text{nn}$, $\lambda^{\max}(0.025, 0.025, 1.0) - \lambda^{\max}(0, 0, 1) \approx 3 \times 10^{-4}$.

In magnetic systems, the development of spin-spin correlations can be observed in the \mathbf{q} -dependent susceptibility, $\chi(\mathbf{q})$. In the Gaussian approximation one has $\chi(\mathbf{q}) \propto (T - \lambda^\alpha(\mathbf{q}))^{-1}$ (see Appendix B). Therefore, the critical mode that minimizes the free energy, $f^{(2)}(T)$, also controls the magnetic correlations as $T \rightarrow T_c$, with T_c given by Eq. (15). In the paramagnetic (PM) regime, $T \gg \theta_{\text{CW}}$, one expects all modes to contribute to $\chi(\mathbf{q})$. This is also the regime in which MFT applies, $T > T_c$, and is expected to provide quantitatively accurate results. Therefore, a build up of PM correlations is understood in terms of an underlying critical mode that marks a transition to an ordered state at T_c . This mean-field

TABLE I: The two maximum eigenvalues and corresponding eigenvectors of $\mathcal{J}(\mathbf{q}_{\text{ord}})$ at $\mathbf{q}_{\text{ord}} = (001)$ for spin ice with Ewald evaluation of the dipolar interactions. The $U^{a,\alpha}(\mathbf{q}_{\text{ord}})$ are normalized eigenvectors, where the weights indicate a two-in (positive value) two-out (negative value) spin ice structure. In particular, the spins on sub-lattices $a = 1$ and $a = 3$ point out of and spins on sub-lattices $a = 2$ and $a = 4$ point in to the tetrahedron.

α	$\lambda^\alpha(\mathbf{q}_{\text{ord}})/D$	$U^{a,\alpha}(\mathbf{q}_{\text{ord}})$
1	3.1575	$\frac{1}{\sqrt{2}}(-1, 1, 0, 0)$
2	3.1575	$\frac{1}{\sqrt{2}}(0, 0, -1, 1)$

approach has been used to study the PM elastic neutron scattering in the $\langle 111 \rangle$ pyrochlores.⁵² For the dipolar spin ice model, one obtains results that are in agreement with the experiments and simulations of $\text{Ho}_2\text{Ti}_2\text{O}_7$ for $R_c > 250\text{nn}$.³³ The best results are found when dipoles are treated with the Ewald technique. If one employs too small a cut-off distance, e.g., much less than $R_c \approx 100\text{nn}$, then one finds that the PM scattering is concentrated in regions of the first zone that are inconsistent with experiments. This is especially true at cut-off distances studied in Refs. 31 and 32. Again, we believe this is a direct consequence of the failure of a finite dipolar sum to much restore the symmetry of the dipolar Hamiltonian, i.e., to produce a quasi-degenerate $\lambda^{\max}(\mathbf{q})$ -spectrum.

From MFT, we can also determined the value of $J_{\text{nn}}/D_{\text{nn}}$ at which the ordering changes from an “all-in–all-out” $\mathbf{q} = 0$ state (i.e., from large negative anti-ferromagnetic J_{nn}) to the (001) long-range ordered spin ice state. We find that the transition between the two states occurs at $J_{\text{nn}}/D_{\text{nn}} = -0.905$. This is in full agreement with the value found in Monte Carlo simulations results for the transition between all-in–all-out $\mathbf{q} = 0$ ordering and spin ice behavior.⁴⁴

Having obtained strong evidence from MFT that there exists a well-defined, unique ordering wave vector in the long-range dipolar spin ice model at the Gaussian level, we can proceed with our search for a dynamically-inhibited transition to long-range order in the model by the use of a conventional Metropolis single spin-flip MC simulation.

IV. DYNAMICAL FREEZING AND LOOP MOVES IN MONTE CARLO SIMULATIONS

A. Dynamical Freezing in Conventional Single Spin Flip Monte Carlo Simulations

The mean field theory results presented in the previous section make it clear that from the point of view of a strictly equilibrium (statistical mechanics) magnetic ordering phenomenon, the dipolar spin ice model of Eq. (2) should be a rather conventional system with a unique and

well defined ordering wavevector and staggered magnetization order parameter. The question then becomes: why don't Monte Carlo simulations of the dipolar spin ice model, or in fact the real spin ice materials themselves, develop the long-range ordered phase predicted by mean field theory? The problem turns out to lie in the local single spin flip dynamics employed within the Metropolis algorithm and, similarly, the local spin dynamics at play in the real materials. As we will show below, Monte Carlo simulations of the dipolar spin ice model using single spin flips experience a dynamical freezing at low temperatures. This arises due to the existence of large energy barriers separating distinct quasi-degenerate spin ice configurations, and prevents the simulation (and the real materials) from finding its true energetically-favored long-range ordered ground state (see Ref. 82 for a related problem).

Observation of the acceptance rate $A(T)$ (percentage of accepted Monte Carlo steps) of the dipolar spin ice simulations makes it immediately apparent that out-of-equilibrium freezing occurs at low temperatures, that is below $T \sim 0.4$ K (as illustrated in Fig. 11a) for the J_{nn} and D_{nn} parameters appropriate for $\text{Dy}_2\text{Ti}_2\text{O}_7$. Fig. 11b shows that $A(T)$ can be parametrized by a Vogel-Fulcher temperature dependence as found in numerous freezing phenomena: $A(T) \propto \exp(\Delta/(T - T_{\text{freeze}}))$, where the freezing temperature, T_{freeze} , is introduced in an *ad hoc* fashion. In Fig. 11b, $\Delta = 1$ K.

It is clear that in order to investigate the existence of a true energetically-favored ground state in the dipolar spin ice model, a standard Monte Carlo simulation employing local single spin flip dynamics is insufficient. Indeed, as Fig. 11 shows, these dynamical processes are frozen-out at T just slightly below 0.4 K for a model of $\text{Dy}_2\text{Ti}_2\text{O}_7$. For J_{nn} and D_{nn} appropriate to describe $\text{Ho}_2\text{Ti}_2\text{O}_7$,³³ the single spin flip Monte Carlo acceptance rate falls below 10^{-6} at a temperature near 0.6 K. Without ascribing any deep significance to it, it is interesting to note that this freezing out in the simulation at 0.4 K and 0.6 K corresponds rather closely to the temperatures at which freezing is found in $\text{Dy}_2\text{Ti}_2\text{O}_7$ ⁴¹ and $\text{Ho}_2\text{Ti}_2\text{O}_7$,⁴⁰ respectively.

This freezing-out occurs due to large free energy barriers separating the (almost) degenerate ice-rules states, which develop rapidly at a temperature of order T_{peak} , and which are associated with introducing a single spin flip to a tetrahedron obeying the ice rules. As discussed above, and further supported by the mean-field calculation, the effective (ferromagnetic) nearest neighbor interaction J_{eff} favors the ice-rules configuration. As the temperature drops the Boltzmann weight $\exp(-4J_{\text{eff}}/T)$ suppresses the probability that a spin flip will take a given tetrahedron into an intermediate, thermally activated non ice-rules obeying configuration. Thus single spin flip Monte Carlo moves are, for all practical purposes, frozen-out and dynamically eliminated within the simulation when $T \ll J_{\text{eff}}$.

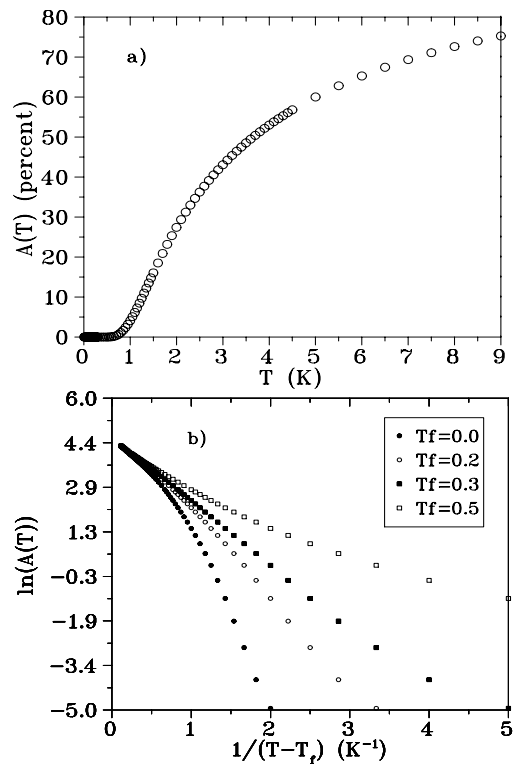


FIG. 11: (a) Single spin flip Monte Carlo step acceptance rate $A(T)$ for a simulation of $\text{Dy}_2\text{Ti}_2\text{O}_7$. The simulation becomes frozen when the acceptance rate falls to zero. (b) The logarithm of the acceptance rate plotted versus inverse temperature, minus some freezing temperature T_{freeze} , follows a Vogel-Fulcher type law.

B. Loop Moves in Monte Carlo Simulations

In order to explore the low temperature ordering properties of dipolar spin ice, one needs a Monte Carlo algorithm with non-local updates that effectively bypass the energy barriers that separate nearly degenerate states and allows the simulation to explore the restricted ice-rules phase space that prevents ordering in the model.^{58,59} In other words, we employ non-local dynamical processes to restore ergodicity in the Monte Carlo simulation, and then use this new algorithm to explore and characterize the long-range ordered state that arises out of ice-rules manifold and which is energetically favored by the dipolar spin ice model.

We first identify the true zero energy modes that can take the near-neighbor spin ice model from one ice state to another exactly energetically degenerate ice state. An example of these zero modes, or loops, is shown in Fig. 1. We take as an initial working hypothesis that in the dipolar spin ice model, with interactions beyond nearest neighbor, the system freezes into an ice-rules obeying state. This is indeed what we found: in all of the tests we performed, systems simulated using conventional single spin-flips always froze-out in an ice-rules obeying

state with no “defects” (by defects we mean violations of the Bernal-Fowler ice rules). With interactions beyond nearest-neighbor, these loop moves become quasi-zero modes that can take the dipolar spin ice model from one ice-rules state to another without introducing spin defects into tetrahedra in the lattice. This allows all of the quasi-degenerate spin ice states to be sampled ergodically, and facilitates the development of a long-range ordered state by the system at low temperatures.

Within the Monte Carlo simulation, we use the Barkema and Newman^{56,57} loop algorithm originally designed for two dimensional square ice models, and adapt it to work in a similar manner on the three dimensional pyrochlore lattice. In the context of square ice, we tested two types of loop algorithms, the so-called *long* and *short* loop moves. In the square ice model, each vertex on a square lattice has four spins associated with it. The vertices are analogous to tetrahedron centers in the pyrochlore lattice. The ice rules correspond to “two spins pointing in, two spins pointing out” at each vertex. In the Newman and Barkema algorithm, a loop is formed by tracing a path through ice-rules vertices, alternating between spins pointing into and spins pointing out of the vertices. A “long loop” is completed when the path traced by the loop closes upon the same spin from which it started. A “short loop” is formed whenever the path traced by the loop encounters any other vertex (tetrahedron) already included in the loop – excluding the dangling tail of spins (Fig. 12).

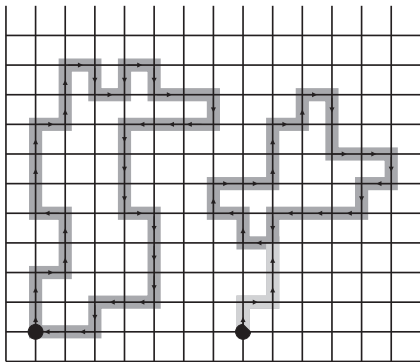


FIG. 12: Long and short loops formed by the Newmann and Barkema algorithm^{56,57} on a square ice lattice. Vertices are represented by points where lattice lines cross. Each vertex has two spins pointing in and two spins pointing out, however for clarity, only spins which are included in the loops are shown. Starting vertices are indicated by large black dots. On the left is an example of a long loop, which is completed when it encounters its own starting vertex. On the right is a short loop, which is complete when it crosses itself at any point. Dark gray lines outline completed loops. The excluded tail of the short loop is shown in light gray.

We now generalize the Barkema and Newmann loop algorithm for our study of the three dimensional pyrochlore lattice spin ice problem. In this system, the smallest com-

plete loop that is a zero mode on the pyrochlore lattice consists of six spins (see Fig. 1). Such a loop was previously identified by Bramwell and Harris²¹ and also by Anderson²² in the context of the spinel lattice. However using the above loop algorithm, much larger loops are possible. When used with the pyrochlore lattice (Fig. 1), such a loop must pass through two spins on each tetrahedron. A loop always “enters” a tetrahedron through an inward pointing spin, and “leaves” a tetrahedron through an outward pointing spin. The periodic boundary conditions of the lattice may also be traversed with no ill consequences. If we form a closed loop in this manner, and each spin is reversed on it, the entire system stays in an ice-rules state. However, small dipole-dipole energy gains or losses may be procured due to small energy differences between the old and the new ice-rules state. These small energy changes caused by the loop moves are evaluated via a Metropolis algorithm within the Monte Carlo. Specifically, a loop move that takes the system from one ice-rules state to another one of lower energy is automatically accepted, while a loop move that takes the system to a higher energy ice-rule state (with energy difference δE between the two states) is accepted with $\exp[-\delta E/(k_B T)] > \text{rnd}$, where rnd is a random number taken from a uniform distribution between 0 and 1.^{56,57}

Before use in a full-scale Monte Carlo simulation, the long and short loop algorithms are subjected to a variety of characterizing tests on the three dimensional pyrochlore lattice.⁵⁹ The first test is a study of the relative speed (measured by CPU time) of the algorithms for different sized lattices. As reported in Ref. 59, it is found that the small loop algorithm creates loops that approach a finite size limit as the system size increases. The long loop algorithm continues creating larger and larger loops, that scale approximately linearly with the number of spins in the simulation cell. This forces the algorithm to become drastically slower for the larger system sizes considered.

Second, tests are carried out to investigate how the two different loop algorithms handle defects that break the ice rules on a tetrahedron. As we know, above the “spin ice peak” in the specific heat of the dipolar spin ice model, the ice rules (two spins pointing into a tetrahedron, two spin pointing out) are generally not obeyed. However, to retain detailed balance, we want our loop algorithm to attempt to form loops at temperatures above the onset of spin ice correlations. The attempt to create a loop is simply aborted in the case where the loop path encounters a defect (either a three-in one-out vertex, or an all-in or all-out vertex). The simulation does not attempt to flip any spins on an aborted loop, and the Metropolis algorithm is not employed in this case. As reported in Ref. 59, the result of ice rules defects on loop algorithm performance is significant. Within the long loop algorithm, the inclusion of only one defect spin per one thousand spins in the system causes almost half of all loops which are attempted to be aborted on the grounds that they have encountered the defect, with efficiency decreasing drasti-

cally as more defects are included. In contrast, the short loop algorithm remains 87% efficient with the inclusion of one defect in one thousand, and retains an efficiency that is much better than the long loop algorithm as more defects are present in the system.⁵⁹

We use both algorithms to perform a true finite temperature Metropolis Monte Carlo simulation of the dipolar spin ice model. We code both algorithms separately, and run simulations using the regular procedure (cooled slowly from a high temperature, equilibrating carefully at every temperature step). Our preliminary Monte Carlo results for both the short and long loop are given in Fig. 13. Even though the data in this figure has low

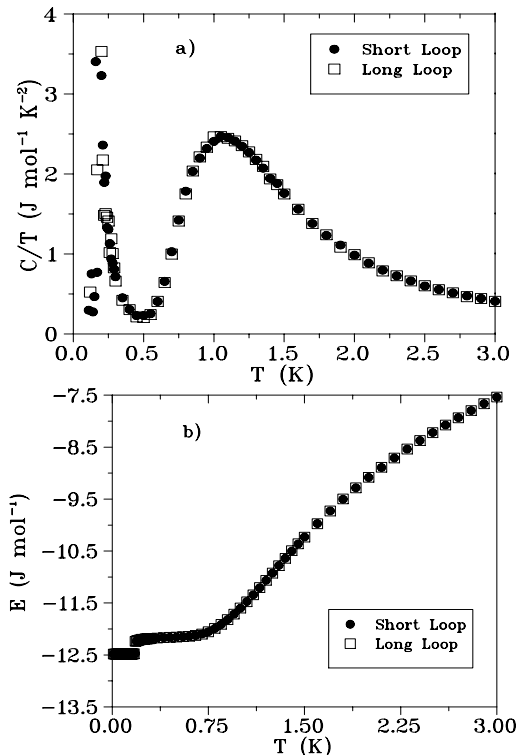


FIG. 13: Preliminary data for the low temperature magnetic specific heat (a) and energy (b) of the dipolar spin ice Monte Carlo, system size $L=3$, with simulation parameters set for $\text{Dy}_2\text{Ti}_2\text{O}_7$. The data represent an average taken over approximately 10^5 production Monte Carlo steps. Closed circles are data from a simulation of the short loop algorithm, open squares are data obtained using the long loop algorithm. Low temperature features are discussed in the next section.

statistics (only 10^5 Monte Carlo production steps per spin), it is clear that both the short and long loops promote roughly the same thermodynamic behavior in the Monte Carlo simulation. The low temperature features (specific heat peak and energy discontinuity at $T \approx 0.2 \text{ K}$) of Fig. 13 are induced in the same manner by both algorithms. These features will be discussed in much more detail in Section V. Since both the long and short loops display equivalent results in the Monte Carlo, we are free

to choose between the two based solely on their performance properties measured above. As alluded to above and detailed in Ref. 59, the short loop algorithm works more efficiently within the requirements of our simulation. However, the disadvantage with using the short loop algorithm is that each loop does not cover as large of a percentage of spins within the lattice. It is not clear to us, without investigating the computational performance (i.e. autocorrelation times) of both algorithms in much more quantitative detail, whether a small number of long loops is better at bringing the system to equilibrium than a larger number of short loops for a fixed CPU time. However, with the additional observation that the long loop algorithm can pass over itself a number of times during its creation, effectively losing additional efficiency in this manner, we ultimately choose to perform the majority of the simulations on the dipolar spin ice model using the short loop algorithm.

With the short loop algorithm chosen for the simulations, we re-investigate the Monte Carlo Metropolis algorithm acceptance rate. Since each loop successfully created (i.e., not aborted by encountering an ice defect) by the short loop algorithm is still subject to rejection by the Metropolis condition on the basis of its change in system energy, we expect the maximum acceptance rate to be somewhat less than the maximum efficiency of the algorithm given above. Results for the loop acceptance rate are shown in Fig. 14. Clearly, the loop algorithm be-

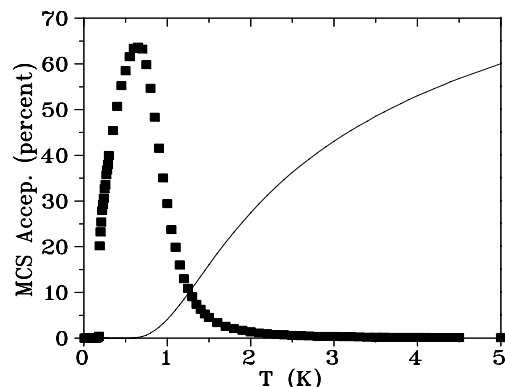


FIG. 14: The Monte Carlo acceptance rate for the short loop algorithm (circles) as compared to the single spin flip algorithm (line), for a simulation using $\text{Dy}_2\text{Ti}_2\text{O}_7$ parameters. Acceptance rates were calculated as percentages of attempted Monte Carlo steps (MCS).

comes effective in the temperature range where the single spin flip algorithm loses its ability to explore all possible configurations of the system. Above about 1 K , the number of accepted loops is very low, due to the fact that the system is not entirely in an ice-rules configuration. As the simulation is slowly cooled, ice-rules constraints begin to develop, and the loop algorithm begins to work efficiently, moving the system between different ice-rules states. In Fig. 14, a sharp drop is observed in the loop

acceptance rate at approximately 0.18 K. As discussed in the next section, this corresponds to the temperature where a phase transition develops in the system, which locks the system into a long-range ordered state and eliminates Monte Carlo dynamics once and for all.

V. LOOP MONTE CARLO INVESTIGATION OF THE TRANSITION TO LONG RANGE ORDER

As suggested by the results above, the short loop algorithm is successful in restoring ergodicity in the simulation. As a consequence of this, we observe a low temperature phase transition in the model. The most familiar and robust indicator of a thermodynamic phase transition (as opposed to dynamical freezing) is a finite size remnant of a singularity (divergence or discontinuity) in the specific heat at the transition temperature T_c . In our simulation of $\text{Dy}_2\text{Ti}_2\text{O}_7$, a sharp cusp in the specific heat is observed at a temperature below the spin ice peak (See Fig. 15a). The feature in the specific heat and the abrupt drop in energy at the same temperature gives good preliminary evidence that the loop algorithm is successful in allowing a phase transition to occur at a temperature of $T_c = 0.18$ K. This is the same temperature where the loop algorithm acceptance rate goes to zero in Fig. 14. The energy curve shows a discontinuous drop at T_c (e.g., latent heat) for large lattice sizes, suggesting a first order phase transition. In the remainder of this section, we attempt to characterize this ordered state, and the phase transition that leads to it. The first step is to identify the order parameter associated with the low temperature ordered state.

Direct inspection of the spin directions at $T < 0.18$ K reveals that the ordered state is a long-range ice-rules obeying state with zero magnetic moment per unit cell and commensurate with the pyrochlore cubic unit cell (see Fig. 4). This state corresponds to the critical mode found above in the mean-field calculation. There are twelve symmetrically equivalent spin configurations for the ground state as explained below, two for each cubic axis direction and their spin reversed states. The ordering wavevector \mathbf{q} lies parallel to one of the cubic axis directions, specifically $\mathbf{q} = (0, 0, 2\pi/a)$ or one of its symmetrically equivalent directions. To construct the ordered state, first consider a starting tetrahedron with its six possible ice-rules states. For a given ordering wavevector \mathbf{q} , this tetrahedron selects one of the four possible spin configurations (two independent configurations and their spin-reversals, $\mathbf{S}_i^a \rightarrow -\mathbf{S}_i^a$) with a total magnetic moment for the tetrahedron perpendicular to \mathbf{q} . The entire ordered state may then be described by planes (perpendicular to \mathbf{q}) of such tetrahedra. The wavelength defined by this \mathbf{q} physically corresponds to antiferromagnetically stacked planes of tetrahedra, which means that a given plane has tetrahedra of reverse spin configuration to the plane above and below it.

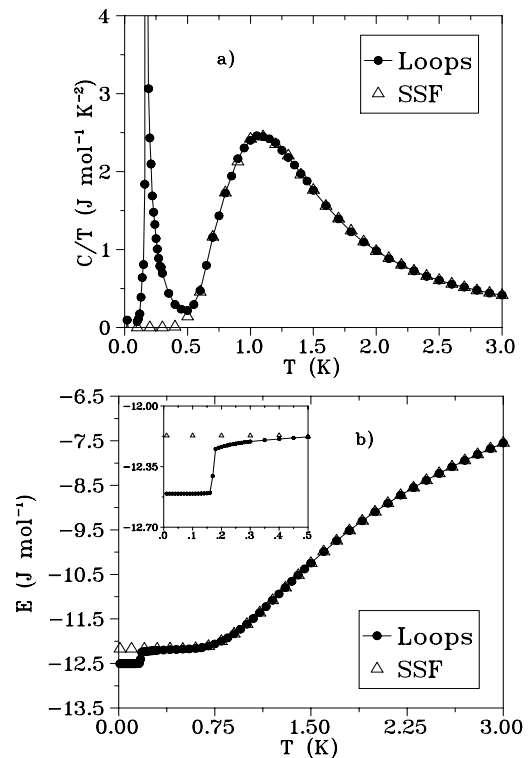


FIG. 15: The low temperature magnetic specific heat (a) and energy (b) of the dipolar spin ice Monte Carlo, system size $L=4$, with simulation parameters set for $\text{Dy}_2\text{Ti}_2\text{O}_7$. Closed circles are simulation data run with the short loop algorithm, open triangles are data obtained using the single spin flip Metropolis algorithm. In the inset of (b), the energy shows an apparent discontinuity at a critical temperature $T_c \approx 0.18$ K. The broad feature in the specific heat at $T \approx 1$ K indicates the rapid development of the spin ice rule obeying states. The sharp feature at T_c is the appearance of a phase transition to a ground state being made (dynamically) accessible via the non-local loop dynamics. Note that these results are of higher statistics than those for Fig. 13, specifically, 1×10^5 equilibration and 3×10^5 production Monte Carlo Steps were used. In addition, the system size is increased to $L = 4$ as opposed to $L = 3$. Also, note that the location of the specific heat peak is at roughly the same temperature and is narrower than for $L = 3$, indicating a finite-size effect on the singular behavior of $C(T)$.

We construct the multi-component order parameter

$$\Psi_\alpha^m = \frac{1}{N} \left| \sum_{j=1}^{N/4} \sum_{a=1}^4 \sigma_j^a e^{(i\phi_a^m + i\mathbf{q}_\alpha \cdot \mathbf{R}_j)} \right|. \quad (16)$$

This type of labeling is natural given that the pyrochlore lattice can be viewed as an FCC lattice with a “downward” tetrahedral basis (Fig. 1). Thus j labels the FCC lattice points of the pyrochlore lattice, and the index a sums over the four spins comprising the basis connected to each j . The index α labels the three possible symmetry related \mathbf{q} ordering wavevectors. For a given \mathbf{q}_α , as de-

scribed above, there are two ice-rules configurations and their reversals which can each form a ground state. Thus $m = 1, 2$ labels these possibilities with the phase factors $\{\phi_a^m\}$, describing the given configurations m . Each Ising variable σ_j^a has a value $+1$ or -1 when a spin points into or out of its downward tetrahedron j , respectively.

As written in Eq. (16), Ψ_α^m has six degenerative components, each of which can take on a value between 0 and 1. Upon cooling through the transition, the system selects a unique ordered configuration, causing the corresponding component of Ψ_α^m to rise to unity and the other five to fall to zero (provided the finite size system is simulated over a time scale less than the ergodic time scale where full spin symmetry is restored). The component which rises to unity is equally likely to be any one of the six, selected by random through spontaneous symmetry breaking.

Fig. 16 is a plot of $\langle\Psi\rangle$ for three system sizes, where

$$\langle\Psi\rangle = \sqrt{\sum_{m=1}^2 \sum_{\alpha=1}^3 (\Psi_\alpha^m)^2} \quad (17)$$

is the magnitude of the multi-component order parameter. These three curves illustrate important finite size effects for $\langle\Psi\rangle$. For $T < T_c$ the different lattice sizes produce identical order parameters. By contrast, $\langle\Psi\rangle$ for the smaller lattice size displays pronounced rounding near T_c and an increased residual value for large T . The larger lattice size produces an order parameter with a clear discontinuity at T_c . This discontinuity in the order parameter combined with the discontinuity of the total energy in Fig. 15b can be viewed as strong preliminary evidence for a first order transition.

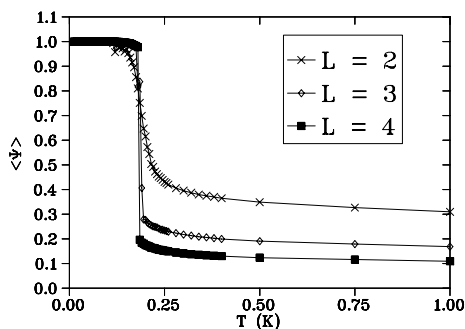


FIG. 16: The $\mathbf{q} = (0, 0, 2\pi/a)$ order parameter. Curves are shown for system size $L = 2$, $L = 3$, and $L = 4$.

We now argue the need to study this phase transition with greater numerical accuracy. This is necessary partially to confirm rigorously its first-order nature. More importantly, once this is done, we want to use the data to confirm the full recovery of Paulings entropy through an estimation of the latent heat released by the transition. To begin, we note that there are a number of criteria at one's disposal to demonstrate the occurrence

of a first-order transition in a Monte Carlo simulation. In particular:

1. The order parameter $\langle\Psi\rangle$ should have a clear discontinuity at T_c .
2. The energy probability histogram, $H(E)$, should have a double peak at T_c , which identifies the coexistence of two distinct phases at T_c .
3. There should be a latent heat at the transition, identifiable by a discontinuity in the internal energy for large system sizes.
4. In the Monte Carlo, the height (maximum) of the specific heat, C_{peak} , and the magnetic susceptibility, χ_{peak} , should be proportional to the simulation volume:

$$C_{\text{peak}}, \chi_{\text{peak}} \propto a + bL^d \quad (18)$$

where a and b are constants and d is the dimension of the lattice, in our case equal to three ($d = 3$).

5. The minimum of the fourth order energy cumulant,⁸³

$$V = 1 - \frac{\langle E^4 \rangle}{3 \langle E^2 \rangle^2} \quad (19)$$

should vary as

$$V_{\text{min}} = V_0 + cL^{-d} \quad (20)$$

where $V_0 \neq 2/3$.

6. The temperature $T_{\text{peak}}(L)$ at which C_{peak} or χ_{peak} have a maximum should vary with the simulation volume as:

$$T_{\text{peak}}(L) = T_c + cL^{-d} \quad (21)$$

where c is a constant, and $T_c = T_{\text{peak}}(L \rightarrow \infty)$.

We have already confirmed the first condition of our list. To check for the second condition the energy probability histogram was calculated by binning the simulation energy values for every Monte Carlo step as the system passes through the transition from higher to lower temperatures (Fig. 17). Above T_c , we observe a single peak Gaussian-like distribution of energies. At T_c , the energy probability distribution shows a double peak, characteristic of the coexistence of two phases found at a first order phase transition. Below T_c we would normally expect to see a Gaussian peak. However, in our case, the histograms below T_c are distorted by the accumulation of energies into the lowest bins due to the proximity of the transition to the ground state. At zero temperature, we expect all of the energies to lie in the bin for the lowest energy.

The next condition on our list is the observation of a latent heat at the transition. Fig. 18 shows the energy

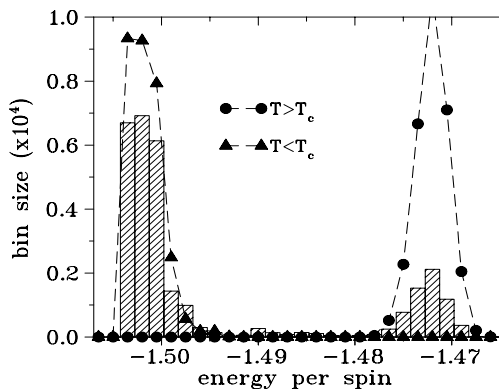


FIG. 17: The energy probability distribution histogram for three temperatures: $T = 0.178$ K, $T = 0.180$ K (T_c), and $T = 0.182$ K. For $T > T_c$ (filled circles), a single peaked Gaussian histogram is present. At the transition temperature (hashed rectangles), a second peak appears which has a lower mean energy. As the temperature falls below T_c (filled triangles), the peak with the higher mean energy disappears, and the system energy eventually gathers in the lowest bin.

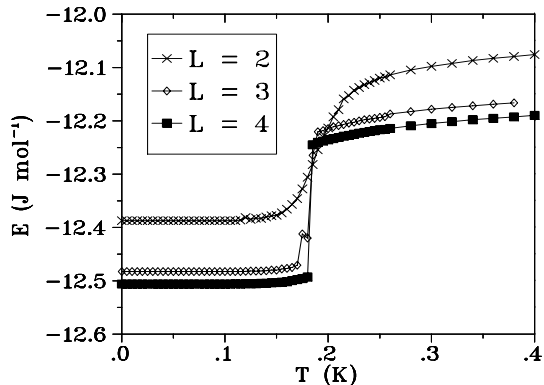


FIG. 18: Details of the simulation energy near the transition for different system sizes.

near the transition for three different system sizes. A clear discontinuity develops as we increase the system size. The energy discontinuity, ΔE , as read off of this graph for $L = 4$, is

$$\Delta E \approx 0.248 \text{ J mol}^{-1}. \quad (22)$$

This behavior is also consistent with the transition being first order. Below, we use this ΔE value in calculating the entropy recovered at the transition (entropy jump). Another calculation of the latent heat at the transition comes from the finite size scaling of condition 4 above.⁸³

$$C_{\text{peak}} \approx \frac{(\Delta E)^2}{4k_B T_c^2} L^d + a \quad (23)$$

where L^d is the system volume as before, and a is the intercept of the graph of $C_{\text{peak}}(L)$ vs. L to test for condition 4, which we now discuss.

When attempting to quantify the relationships in conditions 4, 5 and 6 on our list, we notice a problem. The extremely sharp nature of the transition makes accurate estimates for these quantities almost impossible using a traditional temperature cooled MC simulation of the hybrid single spin flip–loop algorithm. The reason is that the transition temperature region is so narrow, and first-order metastability effects are so strong, obtaining accurate data for quantities such as C_{peak} or V_{min} very near to T_c is extremely difficult. As shown in Fig. 17, the energy probability histogram near a first order transition displays a double hump. The energies that occur between these humps correspond to system configurations that are strongly suppressed by the Boltzmann probability distribution near the transition. We call these “interface configurations”.⁸⁴ Traditional Monte Carlo simulations try to “avoid” these interface configurations as the system is cooled through the transition, because of their suppression by the Boltzmann factor which is the basis of the Metropolis condition. Therefore, the simulation often behaves poorly in this region, moving quickly through interface configurations to find more favorable configurations nearby in configuration space. This can lead to erratic behavior and poor statistics in thermodynamic quantities of interest near the phase transition, thereby reducing the numerical accuracy of the quantities used in finite-size scaling.

To overcome this problem, Berg and Neuhaus⁸⁴ proposed the *multicanonical* method, which is designed to enhance configurations that have energies which occur between the double hump of the probability distribution. If these interface configurations are artificially enhanced, the simulation does not avoid this energy range as strongly and better statistics can be obtained. The version of the multicanonical Monte Carlo algorithm that we use is that proposed by Hansmann and Okamoto,⁸⁵ originally developed to be used in the context of protein folding simulations. The core of the method is:

Perform Monte Carlo simulations in a multicanonical ensemble instead of the usual canonical ensemble. Then, obtain the relevant canonical distribution by using the histogram reweighting techniques of Ferrenberg and Swendsen.⁸⁶ From this, calculate the thermodynamic quantities of interest.

In the multicanonical ensemble, we define the probability distribution by

$$p_{\text{mu}}(E) = \frac{g(E)w_{\text{mu}}(E)}{Z_{\text{mu}}} = \text{constant} \quad (24)$$

where $g(E)$ is the density of states, $w_{\text{mu}}(E)$ is the multicanonical weight factor (not temperature dependent), and Z_{mu} is the associated partition function. The distribution is constant, meaning that all energies have equal weight, which sometimes leads to the name “flat histogram” method. This flatness is important because it ensures that configurations in the interface region of the transition are not suppressed.

Unlike for the canonical ensemble, the multicanonical

weight factor w_{mu} is not *a priori* known. This turns out to be the crucial step of this scheme: finding an accurate estimator of w_{mu} that makes the distribution $p_{\text{mu}}(E)$ flat over the energy range of interest. The details of how to do this are somewhat involved, and will not be explicitly outlined here. The reader is referred to the relevant technical references for details.^{59,85} Our procedure follows that of Ref. 85 very closely.

Assuming that we can find a good estimator of w_{mu} , our method proceeds as follows:

1. We find an accurate estimator of the multicanonical weight factor so that $p_{\text{mu}}(E)$ is reasonably flat over an energy range that includes the transition interface.
2. With this weight factor we perform a multicanonical simulation at one given temperature T slightly higher than T_c .
3. During this simulation run, we gather statistics for the physical variables of choice (for example, the energy E). These variables are weighted according to the multicanonical distribution.
4. From this single simulation, we then obtain the Boltzmann-distributed variables at any temperature for a wide range of temperatures using a reweighting technique.

We use the reweighting technique proposed by Ferrenberg and Swendsen,⁸⁶ which allows us to transform, or reweight, data obtained from another distribution (in our case the multicanonical distribution) to the relevant Boltzmann distribution, at some inverse temperature β . We use this to obtain an estimate for a given physical quantity in the canonical distribution.

We collect data within the multicanonical distribution and use it to calculate the specific heat for the dipolar spin ice model. For the smallest system size considered, we accurately reproduce the specific heat over the transition using the flat histogram method. Fig. 19a shows a comparison between the specific heat of an $L = 2$ system obtained using the histogram method at one temperature, and the traditional Monte Carlo procedure with 8×10^5 equilibration steps and 2×10^6 data production steps for every temperature point. The CPU time that it took to get the histogram data was a small fraction of the time it took to obtain the regular Monte Carlo data. Fig. 19b is a similar result for the next highest system size, $L = 3$. The traditional Monte Carlo data was taken with 5×10^5 equilibration steps and 1×10^6 data production steps. The histogram data was obtained in the same amount of time as for the $L = 2$ data, and it was only slightly more difficult to find a good estimate for $w_{\text{mu}}(E)$. The poor quality of the traditional Monte Carlo Metropolis data for $L = 3$ stands in stark contrast to the smooth data obtained using the multicanonical simulation.

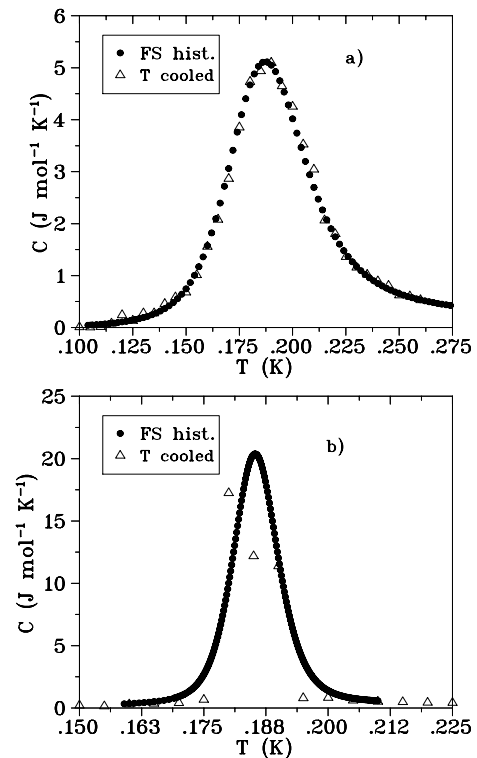


FIG. 19: Specific heat curves over the transition temperature, for $L = 2$ (a) and $L = 3$ (b) system sizes. Closed circles represent data obtained with Ferrenberg and Swendsen’s histogram reweighting technique. Open triangles represent data taken using a traditional temperature cooled Monte Carlo simulation.

Unfortunately, one difficulty with the multicanonical algorithm used here is that, in general, as the system size is increased, it becomes increasingly difficult to obtain a good estimate for a $w_{\text{mu}}(E)$ that would give a flat $p_{\text{mu}}(E)$. The critical temperature, T_c , of the transition seems to be the quantity most sensitive to variations in the flatness of $p_{\text{mu}}(E)$. In contrast, the height of specific heat peak is fairly accurately determined for simulation sizes $L = 2, 3, 4,$ and 5 (Fig. 20), showing only a weak sensitivity to the flatness of $p_{\text{mu}}(E)$.

The aforementioned error associated with T_c for the $L = 4$ peak, as determined from simulations, is of the order of 0.04 K, and becomes increasingly more drastic for the larger system sizes. The variation in the height of the specific heat was found to be much less. Nevertheless, to combat any minor variation in peak height and obtain an accurate finite size scaling results, a statistical average was done on several (~ 10) multicanonical weighting factors to obtain values for C_{peak} . These results are plotted in Fig. 21. A straight line fit to the data using linear regression gives

$$C_{\text{peak}} = 0.8924L^3 - 3.149. \quad (25)$$

The L^3 dependence of $C_{\text{peak}}(L)$ shows that the finite size

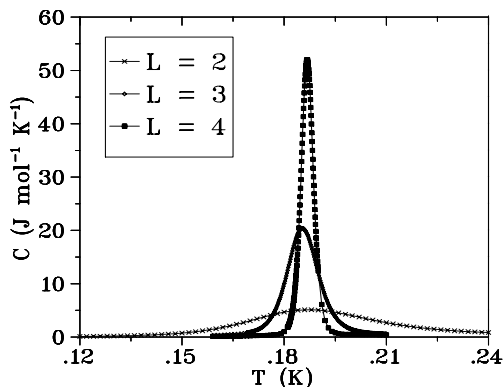


FIG. 20: Specific heat of the transition to long-range order, for system sizes $L = 2, 3$, and 4 . It was found that peak heights for these system sizes did not vary much with the flatness of $p_{\text{mu}}(E)$. Critical temperatures T_c were more sensitive to the flatness of the multicanonical distribution, and hence were harder to estimate than C_{peak} .

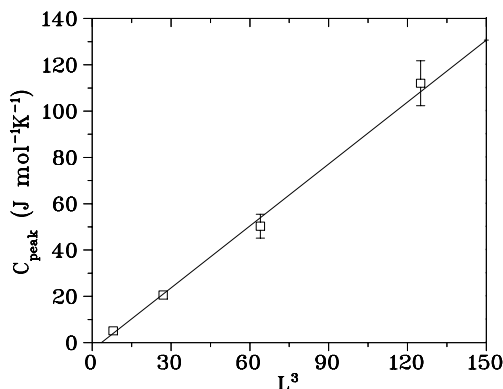


FIG. 21: Finite size scaling fit for the specific peak heights of the ordering transition. Data points represent the mean C_{peak} value for a given L . Error bars show one standard deviation.

scaling is consistent with that expected for a first order transition. Also, as a second estimator of the latent heat, we can use the slope of this line and Eq. (23) to extract ΔE . Doing so we deduce a latent heat of

$$\Delta E = 0.245 \text{ J mol}^{-1}, \quad (26)$$

consistent to within 1% with the value obtained in Fig. 18 (for the $L = 4$ system) from reading directly off of the energy graph (see Eq. (22)).

This completes our study of the nature of the ordering transition in dipolar spin ice. As we have shown, the discontinuity in the order parameter, the release of latent heat, the double peaked energy probability distribution, and the finite size scaling of the specific heat peak all give consistent and compelling evidence for the transition being first order. As the technical details concerning this transition are understood, we can proceed to study where it, and the long-range ordered state which results from

it, stand in our broader picture of ground state entropy found in experiments and in standard single spin flip simulations of the dipolar spin ice model. Since we have confirmed the first order nature of the transition, the configuration of the ordered state, calculated the latent heat, and have reliable data for the specific heat through the transition, we are in a position to re-calculate the total entropy that the dipolar spin ice model releases as it is cooled to low temperatures. This calculation must be done carefully. We know that in an infinite system, a first order transition is characterized by a cusp in the specific heat. If the transition is temperature driven, as in our case, this first order singularity is the latent heat. For an infinite system going through a first order transition, thermodynamics gives

$$\Delta S = \int_0^{T_c^-} \frac{C_{<}}{T} dT + \int_{T_c^+}^{\infty} \frac{C_{>}}{T} dT + \frac{\Delta E}{T}, \quad (27)$$

where $\Delta E/T$ is the latent heat contribution to the entropy (see Fig. 18), and T_c^- and T_c^+ are the temperature limits asymptotically close to T_c , below and above T_c , respectively (see Fig. 18).

To estimate a value for the entropy, we consider the system size $L = 4$ which has good statistical data for the widest temperature range. We integrate the low temperature data for the specific heat in Fig. 20 divided by temperature obtained from the histogram reweighting technique (up to $T \approx 0.21$). For $T > 0.21$ K we use our regular temperature cooled Monte Carlo data (canonical loop + single spin flip) for the integration above this point, and up to 10 K, giving $S(T = 10) - S(T \approx 0) = 5.530 \text{ J mol}^{-1} \text{ K}^{-1}$. To integrate up to $T = \infty$, we follow the same high temperature extrapolation procedure described in Section II, giving $S(T = \infty) - S(T = 10) = 0.145 \text{ J mol}^{-1} \text{ K}^{-1}$. Doing this simple calculation, we find a total recovered entropy of

$$S(T = \infty) - S(T \approx 0) = 5.675 \text{ J mol}^{-1} \text{ K}^{-1}, \quad (28)$$

less than 2% below our expected value of $R \ln 2 = 5.764$. The inset of Fig. 22 clearly shows the entropy recovered by the low temperature transition.

By considering the entropy recovered by the integration of the finite size system specific heat over the transition (inset, Fig. 22), we confirm that it is approximately equal to the value of the entropy we would expect to recover from the latent heat of an infinite system. Using our latent heat calculations above (Eqs. (22) and (26)), this value is approximately $\Delta S_{T_c} = \Delta E/T_c \approx 0.2465/0.180 = 1.37 \text{ J/mol K}$, in good agreement with the jump in $S(T)$ in the inset of Fig. 22.

Taking all indicators together, we have demonstrated here that the transition to long range order at 180 mK recovers all residual Pauling entropy of the dipolar spin ice model. Thus we can assert that the degeneracy associated with the spin ice model, and the corresponding value of zero point entropy, is lifted due to perturbations beyond nearest neighbor dipole-dipole interactions,

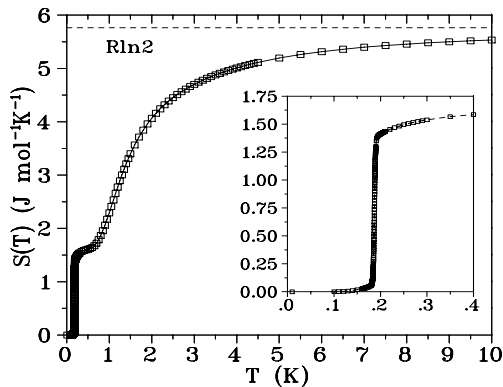


FIG. 22: The entropy calculated from integrating the simulated specific heat, as explained in the text. The entire value of entropy for the system ($R \ln 2$) is recovered in the high temperature limit. The inset shows the details of the entropy recovered by the transition to long-range order.

if equilibrium can be maintained at sufficiently low temperatures.

We comment here on a detail we neglected to discuss above regarding the relationship between the mean-field theory and the results from the loop Monte Carlo simulations. In the Gaussian mean-field theory presented above the calculation that was performed was in effect an identification of the soft-mode against which the paramagnetic phase becomes locally unstable upon cooling. The Monte Carlo simulation finds, however, that the thermodynamic transition to that ordered state is actually first order and occurs before the supercooled critical temperature is reached.

To summarize our results for this section, we refer the reader to the dipolar spin ice Monte Carlo phase diagram, Fig. 5. As illustrated there, the transition between the spin ice phase (which retains Pauling’s entropy) and the $\mathbf{q} = (0, 0, 2\pi/a)$ ordered phase is independent of the strength of J_{nn} . This is consistent with our understanding that the long range order results from perturbative interactions beyond nearest neighbor, caused by the long-range dipolar interaction. This is also what mean-field theory finds in the spin ice regime ($J_{nn}/D_{nn} > -0.905$). We find that this first order line also slightly runs up the boundary between the antiferromagnetic ordered phase and the higher temperature paramagnetic phase, and that a tricritical point separates these two regions of the line, and occurs near the value $J_{nn}/D_{nn} \sim -1.1$.

Due to the near-vertical nature of the phase boundaries in this region, simulations run at a finite T and varying J_{nn} help better map out the low temperature phase lines of interest. However, using this method, we observed that the simulations could easily get “stuck” in the previous spin configuration (either spin ice disordered, $\mathbf{q} = (0, 0, 2\pi/a)$ or AF $\mathbf{q} = 0$) when crossing the vertical phase boundary. This history dependence is illustrated in the phase diagram as hystere-

sis at low temperatures, mainly between the long-range ordered $\mathbf{q} = (0, 0, 2\pi/a)$ and antiferromagnetic $\mathbf{q} = 0$ phases. Regardless of this difficulty, we have confirmed from direct Ewald energy calculations at zero temperature that the true zero-temperature phase boundary between the $\mathbf{q} = (0, 0, 2\pi/a)$ and the AF $\mathbf{q} = 0$ phases lies at $J_{nn}/D_{nn} = -0.905$, in agreement with the result found above in the mean field calculations.

VI. DIPOLAR SPIN ICE IN MAGNETIC FIELD

A very interesting problem that pertains to dipolar spin ice materials is their behavior in an external magnetic field, \mathbf{h} . A number of recent experiments^{60,61,62,64,80} have shown a rich variety of new behavior when spin ice materials are subjected to such a field, which warrants some theoretical investigation.^{63,87} Although not all of the relevant experiments can be described in this short section, we briefly outline some of the most important, referring the reader to the bibliography for further details on their methods and results.

The first experiments on spin ice materials in an applied magnetic field were performed by Harris *et al.*²⁰ In a neutron scattering experiment, they applied a magnetic field of strength 2 T along the [110] direction of a single crystal of $\text{Ho}_2\text{Ti}_2\text{O}_7$, and looked for signs of ordering. They found scattering intensity features which suggest evidence of two ordered magnetic structures, the so-called $\mathbf{q} = 0$ and $\mathbf{q} = X$ phases (Fig. 23). As we will see below, these ordered structures are of fundamental importance in our study of the ground states of the dipolar spin ice model.

A quite interesting set of experiments was performed by Ramirez *et al.*²⁹ and Higashinaka *et al.*,⁸⁸ who subjected polycrystalline samples of $\text{Dy}_2\text{Ti}_2\text{O}_7$ to a variety of different field strengths. Ramirez presented evidence of field-dependent phase transitions in a powder sample, manifested as sharp features in the specific heat at

1. 0.34 K for $h > 1\text{T}$
2. 0.47 K for $1\text{T} \lesssim h \lesssim 3\text{T}$
3. 1.12 K for $h \neq 0$

where we have used h to represent the magnitude of the applied field \mathbf{h} . Higashinaka and co-workers reproduced the basic features of Ramirez’ results down to $T \cong 0.38\text{K}$,⁸⁸ confirming the existence of the two higher-temperature peaks only. The search for a microscopic explanation of these three peaks has been a driving force behind much of the experimental and theoretical work in this field over the past few years, and we discuss it further in the work that follows below.

Another significant experimental study is the measurement of the single crystal magnetization curves (M vs. \mathbf{h}) for the spin ice materials. Fukazawa *et al.* performed a number of experiments on single crystals of

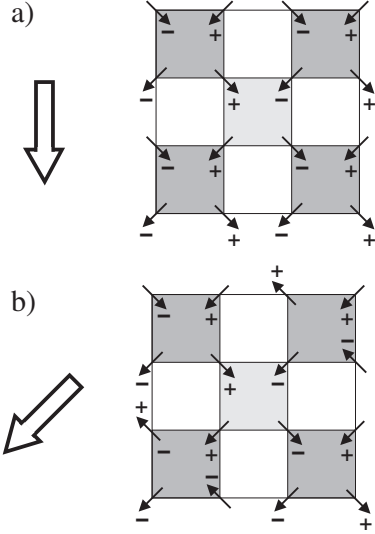


FIG. 23: The pyrochlore unit cell projected down the z -axis. The symbols $+$ and $-$ represent the z component of the spin “head”. Configurations are (a) $\mathbf{q} = 0$ and (b) $\mathbf{q} = X$. The large arrows point in the (a) $[100]$ and (b) $[110]$ directions, and are included to aid in the discussion of ground states in the next section. Note that $\mathbf{q} = X$, although similar, is a spin ice state distinct from the $\mathbf{q} = (0, 0, 2\pi/a)$ ordered state shown in Fig. 4. Specifically, the chains of spins parallel to the $[100]$ direction are staggered antiferromagnetically in the zero field $\mathbf{q} = (0, 0, 2\pi/a)$ ground state (Fig. 4), while they are ferromagnetically correlated and parallel to the field in the $\mathbf{q} = X$ state of (b) above.

$\text{Dy}_2\text{Ti}_2\text{O}_7$, obtaining magnetization curves for the different applied field directions and a range of temperatures.⁶⁰ They showed that magnetization data at 2 K was consistent with the behavior predicted by the spin ice model, in particular the limiting field (large \mathbf{h}) values of the magnetic “anisotropy” (which we illustrate below). Very recently, measurements^{61,64} of the magnetization curves for $\mathbf{h}/[111]$ (read “ \mathbf{h} parallel to the $[111]$ crystal direction”) have uncovered a novel macroscopically degenerate state corresponding to ice-like behavior on the kagome planes in the pyrochlore lattice.^{63,87}

We take into account the applied magnetic field \mathbf{h} in the dipolar spin ice model with a simple term added to the Hamiltonian (Eq. (2)),

$$H' = - \sum_i \mathbf{h} \cdot \mathbf{S}_i^a = - \sum_i (\mathbf{h} \cdot \hat{z}^a) \sigma_i^a. \quad (29)$$

We work strictly with a classical Ising model and neglect any transverse field effects and perturbative changes to the moments arising in a strong field. In this classical approximation, the field \mathbf{h} couples to the spins through the simple scalar product Eq. (29). That is, we neglect small corrections to the energy coming from the very small,

though finite, local susceptibility perpendicular to the (111) direction. As well, we neglect quantum mechanical transverse-field effect that would arise from admixing the doublet ground state wavefunctions with that of the excited crystal field levels. For $\text{Ho}_2\text{Ti}_2\text{O}_7$ and $\text{Dy}_2\text{Ti}_2\text{O}_7$, the first excitation gap is (very roughly) $\Delta \sim 300$ K.²⁸ For the magnetic moments of approximately $10 \mu_B$ for both Ho^{3+} and Dy^{3+} , this means a ground state Zeeman energy splitting of 12.8 K/Tesla. One can therefore safely neglect magnetic field, exchange and dipole-dipole induced admixing for fields less than 10 Teslas, assuming the worse case scenario where the excited doublet also split by about 10 K/Tesla.

To gain a theoretical understanding of the experimental behavior mentioned above, several insightful calculations are possible, using only this simple classical Hamiltonian and a knowledge of the possible ground states of Fig. 23. First, a geometrical understanding of how the magnetic field couples to classical spins on the pyrochlore lattice is desirable. We expect that application of a magnetic field along the three principle symmetry axes of the crystal will result in different spin-field coupling behavior. To explore this, we begin by considering the non-interacting limit ($\hbar \rightarrow \infty$ or $J_{nn}, D_{nn} \rightarrow 0$). In this case, the only constraints on the spins is the local (111) anisotropy and the coupling with the magnetic field. We can gain more insight by viewing a projection of a tetrahedron down the cubic z -axis as in Fig. 24.

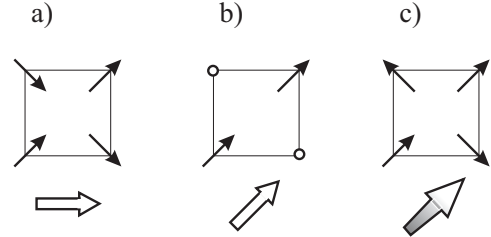


FIG. 24: A single tetrahedron projected down the z -axis. Field directions are (a) $\mathbf{h}/[100]$, (b) $\mathbf{h}/[110]$, (c) $\mathbf{h}/[111]$, depicted by the large arrow outline. Small arrows represent dipole moments coupled to the field. Empty circles represent decoupled spins.

For $\mathbf{h}/[100]$, all four spins on a given tetrahedron are coupled to the field (i.e. all four have a non-zero dot product in Eq. (29)). The expected lowest energy configuration in the absence of spin-spin interaction is the one where all spins have their $[100]$ components aligned with the field. Knowing this, we can calculate the $h \rightarrow \infty$ value for the M vs. \mathbf{h} curves by considering the average moment M (in units of Bohr magneton per rare earth ion, μ_B/R^{3+}), in the direction of the field $\mathbf{h}/[100]$:

$$\begin{aligned} M(\mathbf{h} \rightarrow \infty) &= \frac{1}{4\sqrt{3}} ([111] + [1\bar{1}\bar{1}] + [1\bar{1}1] + [11\bar{1}]) \cdot [100] \cdot \mu \end{aligned}$$

$$= \frac{1}{\sqrt{3}} \cdot \mu \cong 0.5774 \cdot \mu. \quad (30)$$

Also, to calculate M in the appropriate units (μ_B/R^{3+} , measured in experiments) one must include the factor μ , which is the magnetic moment of the appropriate rare earth ion. If R is Dy^{3+} or Ho^{3+} , $\mu \approx 10\mu_B$. Note that, from Fig. 24a, this lowest energy spin-field coupled state is compatible with the ice rules. If we decorate the entire lattice with tetrahedra such as this, we recover the $\mathbf{q} = 0$ state of Fig. 23a. This suggests that this ordered state should be one of the ground states for the interacting dipolar spin ice model, with a sufficiently strong external field $\mathbf{h}//[100]$. Indeed, this order has been observed experimentally⁸⁰ on samples of $\text{Dy}_2\text{Ti}_2\text{O}_7$.

For $\mathbf{h}//[110]$, only two of the four spins on a tetrahedron couple to the field. One expects that, with precise alignment of the sample, these other two spins would remain decoupled even in the application of high magnetic fields. These decoupled spins are thus free to choose an ordering pattern that satisfies their dipolar interaction. Because of the complexity of the dipolar interaction, the ground state spin configuration is not immediately obvious from studying the geometry. However, one expects any zero-temperature phase to be consistent with the ice-rules (see Fig. 24b). In the limit of very high applied field and perfect sample alignment, one expects the magnetization to approach

$$\begin{aligned} M(\mathbf{h} \rightarrow \infty) &= \frac{1}{2\sqrt{3}} ([111] + [1\bar{1}\bar{1}]) \cdot \frac{1}{\sqrt{2}} [110] \cdot \mu \\ &= \frac{1}{\sqrt{6}} \cdot \mu \cong 0.4082 \cdot \mu. \end{aligned} \quad (31)$$

Finally, for $\mathbf{h}//[111]$, all four spins on a tetrahedron are coupled to the field. An interesting complication arises in this case due to crystal geometry; any high-field phase of the material will be inconsistent with the ice-rules, and the spins will form a *three-in one-out* (or its spin reverse) tetrahedral configuration (Fig. 24c). For zero temperature, both the long-range ordered ice-rules state and the three-in one-out state will exist for different field strengths. For low magnitudes of \mathbf{h} , we expect a competition between the exchange, dipolar and magnetic field parts of the Hamiltonian. At low enough temperatures, one predicts^{59,61,63,64,87} that a plateau will develop in the magnetization curve due to the tendency of each tetrahedron to stay in the ice rules up to a critical field. If we couple three of the spins to the magnetic field, and leave one to oppose the field but obey the ice rules, we find a magnetization of

$$\begin{aligned} M(\mathbf{h} = \text{“small”}) &= \frac{1}{4\sqrt{3}} ([111] + [\bar{1}11] + [1\bar{1}\bar{1}] + [\bar{1}\bar{1}\bar{1}]) \cdot \frac{1}{\sqrt{3}} [111] \cdot \mu \\ &= \frac{1}{3} \cdot \mu \cong 0.3333 \cdot \mu. \end{aligned} \quad (32)$$

In the limit of very high applied field, we expect the spin that is coupled anti-parallel to the field (in the case

above, the last spin vector $[\bar{1}\bar{1}\bar{1}]$) to break the ice rules, in favor of minimizing its energy with respect to the field. In this case the high field magnetization is

$$\begin{aligned} M(\mathbf{h} \rightarrow \infty) &= \frac{1}{4\sqrt{3}} ([111] + [\bar{1}11] + [1\bar{1}\bar{1}] + [11\bar{1}]) \cdot \frac{1}{\sqrt{3}} [111] \cdot \mu \\ &= \frac{1}{2} \cdot \mu = 0.5 \cdot \mu. \end{aligned} \quad (33)$$

We find that our Monte Carlo is successful in reproducing the high field limiting values of the experimental M vs. \mathbf{h} curves.⁶⁰ In addition, we find that the Monte Carlo also reproduces the plateau expected for $\mathbf{h}//[111]$ and low temperatures.⁵⁹ However, because these large \mathbf{h} results are easily obtainable for a nearest-neighbor spin ice model ($D_{\text{nn}} \rightarrow 0$), we won't discuss them further in this work. The reader is referred to Ref. 59 and Ref. 60 for the detailed results of this study.

A numerical calculation of interest that is easily performed is the Ewald energies of the various ground state configurations that we have encountered so far in the dipolar spin ice model. The spin ice configurations that we consider are both the $\mathbf{q} = 0$ and $\mathbf{q} = X$ phases identified by Harris,²⁰ and the $\mathbf{q} = (0, 0, 2\pi/a)$ ground state identified previously in this work (Fig. 4). In addition, we expect a “three-in one-out” state to become the lowest energy state for some critical field along the $\mathbf{h}//[111]$ direction. Figs. 25 and 26 are the results of these ground state energy calculations for a system size $L=2$ and parameters appropriate for $\text{Ho}_2\text{Ti}_2\text{O}_7$ ($J_{\text{nn}} = -0.52\text{K}$, $D_{\text{nn}} = 2.35\text{K}$). As expected, we find the same qualitative behavior for calculations involving $\text{Dy}_2\text{Ti}_2\text{O}_7$ parameters. In addition, because all of the ground state configurations considered are commensurate with the unit cell of the pyrochlore lattice, these calculations scale trivially for sizes $L > 2$.

Fig. 25a confirms that the $\mathbf{q} = 0$ configuration becomes the lowest energy state for large field strength ($h > 0.034$ T) for $\mathbf{h}//[100]$, as expected from simple geometrical considerations. Recall that in the $\mathbf{h}//[110]$ case, there exist two decoupled spins per tetrahedron, and subsequently no lowest-energy configuration is obvious from the geometric field coupling Eq. (29). However, one may anticipate that for $\mathbf{h}//[110]$, the decoupled spins (Fig. 24b) order in “chains” perpendicular to the $[110]$ direction, arranged in such a way as to partially satisfy the dipolar interaction. We find that this is precisely the $\mathbf{q} = X$ state, which Fig. 25b shows to be the lowest energy state at for $h > 0.023$ T.

Consequently, Fig. 25b has direct relevance to experiments by Fennel *et al.* and Hiroi *et al.* that were performed on $\text{Dy}_2\text{Ti}_2\text{O}_7$ with a magnetic field $\mathbf{h}//[110]$.^{62,80} Fennel *et al.* observed neutron diffraction patterns that showed Bragg scattering at $\mathbf{q} = 0$ “points” and diffuse scattering at $\mathbf{q} = X$ “points”, but no true $\mathbf{q} = X$ long-range order. They suggested that this behavior would arise from long-range ferromagnetic order occurring in field-coupled spin chains (called α chains by Hiroi⁶²),

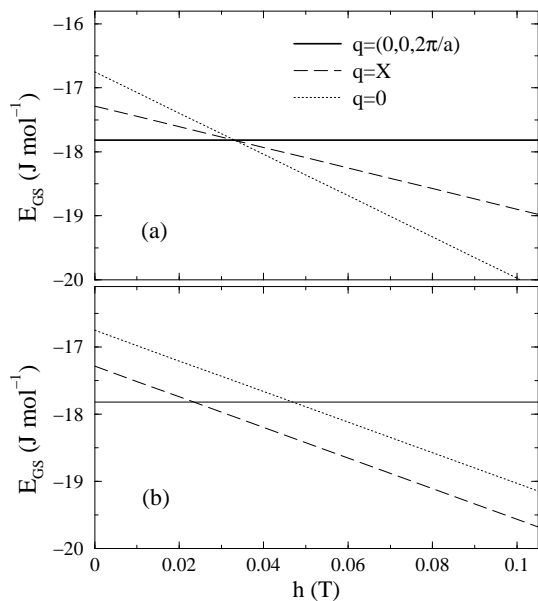


FIG. 25: The $T=0$ energies per spin of the three ice-rules ordered states of the dipolar spin ice model, as a function of applied internal field $h = |\mathbf{h}|$ along the (a) [100] and (b) [110] directions for $J_{nn} = -0.52$ K and $D_{nn} = 2.35$ K (i.e. $\text{Ho}_2\text{Ti}_2\text{O}_7$ parameters).

and short-range “antiferromagnetic” order occurring in the field-decoupled spin chains (β chains).⁸⁰ In this argument, the true ground state is a $\mathbf{q} = X$ structure that is dynamically inhibited from being accessed on experimental timescales.

Specific heat measurements by Hiroi *et al.* were used to extract the specific heat contributions of both the α chains and the β chains.⁶² They suggest that the specific heat due to the β chains resembles that which one would expect for a low-dimensional spin system without long-range order. They also argue for the presence of geometrical frustration in the triangular sub-lattice that contains the β chains. If such a frustration exists, it might be expected to destabilize the “antiferromagnetic” correlations between these chains that would otherwise lead to $\mathbf{q} = X$ order. Therefore, Hiroi *et al.* argued against true long-range order for the system, rather that the β chains become effectively isolated and behave as “pure” one-dimensional ferromagnetic systems without long-range order in the ground state.

At this point, Fig. 25b is consistent with the idea of long-range $\mathbf{q} = X$ order for the dipolar spin ice model with a magnetic field $\mathbf{h} // [110]$. As we will discuss below, finite-temperature Monte Carlo calculations on the dipolar spin ice model also support the idea that, similar to the development of $\mathbf{q} = (0, 0, 2\pi/a)$ order in the zero-field case, the development of $\mathbf{q} = X$ order for $\mathbf{h} // [110]$ may in some cases be dynamically inhibited in experimental systems with local spin dynamics. The failure of the frustration of the β chain sub-lattice invoked by Hi-

roi *et al.*⁶² to destroy the long-range $\mathbf{q} = X$ order may be another example of the small energy scale left over by the infinite-range dipole-dipole energy (Eq. (2)), and why such interactions must be handled carefully using techniques such as the Ewald method.

It should also be noted here that the $\mathbf{q} = 0$ and $\mathbf{q} = X$ lines are parallel in Fig. 25b *only* for samples that are perfectly aligned with \mathbf{h} along the [110] crystal axis. This is an important phenomenon one must consider when comparing theory and experiment, as only a small crystal misalignment will partially couple spins on the β chains to the field. Because *precise* alignment of a crystal is often very difficult, the possibility of misalignment of the order of a degree must be taken into consideration when studying single crystal data with $\mathbf{h} // [110]$. Repeating our ground state energy calculation for misalignment of one degree along the [100] direction, one finds a crossing of the $\mathbf{q} = X$ and $\mathbf{q} = 0$ lines in Fig. 25b at about 1.3 T, the $\mathbf{q} = 0$ configuration being of lowest energy above this field strength.⁶⁰

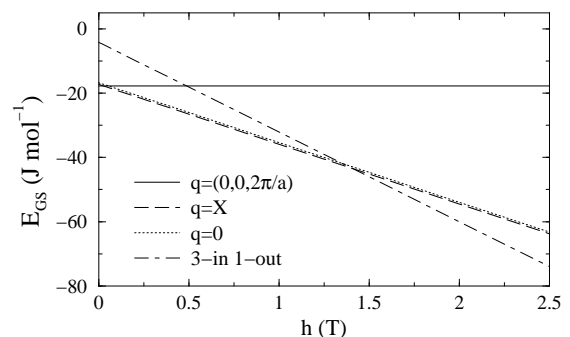


FIG. 26: The $T=0$ energies per spin of the three ice-rules ordered states and the three-in one-out spin state of the dipolar spin ice model as a function of applied internal field \mathbf{h} along the [111] direction. The $\mathbf{q} = X$ state becomes the ground state at 0.029 T. The three-in one-out configuration becomes the ground state at around 1.4 T, breaking the ice rules for each tetrahedron. The $\mathbf{q} = X$ line is always 0.534 J mol⁻¹ below the $\mathbf{q} = 0$ line at any given field.

Also, as Fig. 26 confirms, the three-in one-out spin configuration become the lowest energy state for large $\mathbf{h} // [111]$. Interestingly, the $\mathbf{q} = X$ state is the ground state for $0.029 < h < 1.4$ T. This is consistent with the idea that that the z component of the field for the [111] direction gives a zero net Zeeman contribution to the unit cell for both the $\mathbf{q} = 0$ and $\mathbf{q} = X$ spin configurations. Therefore, the only energy scale difference left over between the two states comes from the [110] component of the field, meaning that $\mathbf{q} = X$ will be slightly lower in energy than $\mathbf{q} = 0$ (as in Fig. 25b) for all $\mathbf{h} // [111]$. Most other features of the $\mathbf{h} // [111]$ field (such as the intermediate-field plateau and the high-field breaking of the ice-rules) are readily explainable in a nearest-neighbor spin ice model without dipolar interaction, hence we will discuss them no further in this work.

We now turn to a set of preliminary results of finite-temperature Monte Carlo simulations for the dipolar spin ice model in a magnetic field. As mentioned previously, the desire to explain the three field-independent specific heat peaks^{29,88} of polycrystalline $\text{Dy}_2\text{Ti}_2\text{O}_7$ has driven much of the experimental and theoretical interest in this field over the past few years. Ramirez *et al.* were the first to suggest²⁹ that some of these peaks can be attributed to a fraction of crystallites whose [110] axes happen to align (closely) with the applied magnetic field. More generally, we can interpret this argument as saying that magnetic moments which are not strongly coupled to the magnetic field through Eq. (29) are free to contribute to a dipole-induced phase transition (and therefore sharp peaks in the specific heat) at low temperatures. Historically, the $\mathbf{h}/[110]$ coupling of Fig. 24b was considered to be the most likely scenario to provide these field-decoupled spins in a finite number of crystallites in the polycrystalline sample.²⁹ However, one may in fact argue that crystallites with only *one* field-decoupled spin would occur in much greater number in a real polycrystalline sample. This is due to the fact that, for a given crystallite orientation, there are an infinite number of applied magnetic field directions for which a given sub-lattice is decoupled (one of these being $\mathbf{h}/[112]$ ⁶¹), corresponding to a rotation degree of freedom in the choice of \mathbf{h} that does not exist in the two spin field-decoupled case ($\mathbf{h}/[110]$).

Hence, we carry out finite-temperature Monte Carlo simulations on the dipolar spin ice model for various field directions to look for signs of an ordering transition in the specific heat. In the case of $\mathbf{h}/[100]$ and $[110]$, the ground state is known and hence an order parameter can be constructed, facilitating the identification of any possible phase transitions. We perform simulations on the spin ice model with the added term Eq. (29), employing both single spin flips and loop moves (and ignoring the demagnetization effects discussed in Appendix C). For fields parallel to the $[110]$ crystal axis, of magnitude large enough to favor the $\mathbf{q} = X$ ground state, but still relatively small, we found that the simulations were able to find this fully ordered state only when the loop moves were employed (see Fig. 27). This can be understood by studying the structure of the $\mathbf{q} = X$ state and its coupling to this field direction, as shown in Figs. 23b and 24b. As discussed above, the field-decoupled spins occur in long chains (β chains) in the bulk material. Within a single β chain, spins tend to point ferromagnetically along one direction as dictated by the exchange and magnetic field energies. In addition, the dipolar term weakly couples nearby chains, and in order to minimize this coupling energy, neighboring chains can be expected to seek out a unique ordering pattern. However, to explore different chain-orientations at lower temperatures, whole chains must be flipped at once in the simulation (imagine going from the $\mathbf{q} = 0$ state to the $\mathbf{q} = X$ state in Fig. 23). Thus, if the system is attempting to settle into the $\mathbf{q} = X$ state at a temperature well below the onset of ice-rules correlations, these global chain-flip moves must be em-

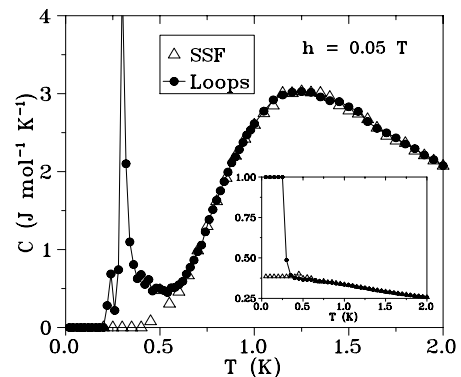


FIG. 27: The specific heat of $\text{Dy}_2\text{Ti}_2\text{O}_7$ for $\mathbf{h}/[110]$, obtained using simulations with single spin flips and loop moves. Inset: the $\mathbf{q} = X$ order parameter calculated by the simulations. The single spin flips (SSF) are unable to find the true ground state of the system, while the loops moves (Loops) allow the system to order into the $\mathbf{q} = X$ structure. The large value of the high-temperature tail of the order parameter is a finite-size effect.

ployed in the simulation. Luckily, such chain-flip moves are a subset of the generic loops created in the Monte Carlo loop algorithm (due to periodic boundary conditions), and thus no major modification of the simulation procedure is needed.

As we see in Fig. 27, there is evidence of a feature in the specific heat that corresponds to the temperature where the $\mathbf{q} = X$ order parameter jumps to essentially the saturation value of one. The feature in the specific heat and the corresponding jump in the $\mathbf{q} = X$ order parameter are at approximately 0.3 K, show that this is not the same transition as the $\mathbf{q} = (0, 0, 2\pi/a)$ transition of the previous section. For small applied field, the transition temperature depends on the strength of the applied magnetic field. For example, at 0.075 T the transition temperature moves up to 0.4 K, and requires the loop moves to be manifest. For fields of the order of 0.01 T and larger, the transition has risen to high enough temperatures that single spin flip dynamics are still sufficiently present to promote development of the ground state, without help from the loop moves. Details of this are illustrated in Fig. 28. Note that the phase transition illustrated in these two figures appears to be strongly first order, and hence obtaining good error control is difficult with the current statistics (8×10^4 equilibration and 8×10^4 production MC steps). A more detailed study employing multicanonical techniques is currently in progress to look more closely at the exact temperature and field dependence of this new phase transition.

This sharp specific heat feature persists to a magnetic field value of $h \sim 0.15$ T. At higher field strengths, the singularity broadens and gets absorbed into the spin ice peak of the specific heat at $T \sim 1.2$ K. However, for all $h > 0.5$ T, the order parameter is observed to jump to unity at around 0.9 K, which appears to be the saturation

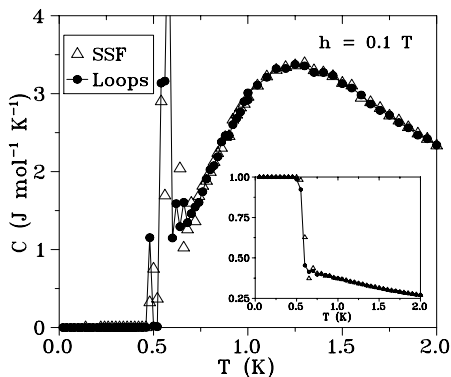


FIG. 28: The specific heat of $\text{Dy}_2\text{Ti}_2\text{O}_7$ for $\mathbf{h}//[110]$, obtained using simulations with single spin flips and loop moves. Inset: the $\mathbf{q} = X$ order parameter calculated by the simulations. Both the single spin flips and the loop moves are able to find the true $\mathbf{q} = X$ ground state of the system.

value for very strong fields. Hence, although the nature of the transition to long-range order changes at some field $h \sim 0.15$ T, the fact remains that the simulations can always find the $\mathbf{q} = X$ ground state up to infinite field values.

For larger field values ($h > 0.2T$) and $\mathbf{h}//[110]$, we reproduce the experimental⁶² features of the specific heat for $\text{Dy}_2\text{Ti}_2\text{O}_7$ nicely. Fig. 29, which shows our results for $0 < T < 8$ K for several field values, is relegated to Appendix C where we discuss demagnetization effects. Comparing this figure to Fig. 2, Ref. 62, shows that our model quantitatively reproduces the development of two peaks as h is increased above 0.5 Tesla. The $T \sim 7$ K peak, clearly visible for $h = 1.0$ T (Fig. 29d), is a Schottky-type peak which corresponds to the freezing of field-coupled (α) spin chains that are along $[110]$.⁶² The lower peak at $T \sim 1$ K is attributed to the development of long-range correlations between β -chains, however its exact relationship to the ordering of the model as observed by the jump in the $\mathbf{q} = X$ order parameter is still under study.

Finally, we performed finite-temperature Monte Carlo simulations on the dipolar spin ice model for fields parallel to the $[100]$, $[111]$ and $[112]$ crystal directions. In particular, we used field strengths larger than those which would favor $\mathbf{q} = (0, 0, 2\pi/a)$ order (see Figs. 25 and 26). In the case of $\mathbf{h}//[100]$, we see the gradual development of $\mathbf{q} = 0$ long-range order as the simulation cools down through the spin ice peak, and no sharp singularities in the specific heat which may signal a phase transition. Simulations for $\mathbf{h}//[111]$ also shows no unexpected anomalies in the specific heat. Interestingly, work on the $\mathbf{h}//[112]$ case has not yet produced any signs of an ordering transition in the field-decoupled spin sub-lattice, as one might expect from our discussion above. Work addressing this problem is ongoing.

To summarize this section, we have performed several

calculations of the properties of the dipolar spin ice model in an external magnetic field. Ewald energy calculations of various spin configurations reveals the preferred $T = 0$ ordering for various field directions. In particular, for $\mathbf{h}//[100]$ the $\mathbf{q} = 0$ structure is the ground state, while for $\mathbf{h}//[110]$ we find the $\mathbf{q} = X$ state becomes energetically favored. For finite-temperature Monte Carlo simulations of the dipolar spin ice model, we find that the system settles into these ground states for the respective field directions, although non-local dynamics are needed to find the $\mathbf{q} = X$ state for $\mathbf{h}//[110]$ at low fields. We also predict a sharp first-order phase transition to the $\mathbf{q} = X$ state and a corresponding specific heat spike for $0.02 < h < 0.15$ T in $\text{Dy}_2\text{Ti}_2\text{O}_7$. Interestingly, unlike the transition to the $\mathbf{q} = (0, 0, 2\pi/a)$ state in zero field, the transition to the $\mathbf{q} = X$ state *can* be found with single spin flips in the Monte Carlo for fields $0.10 < h < 0.15$ T, although it is unknown whether local dynamics will be manifest in the corresponding range in a real experiment. Finally, for $h > 0.15$ T and parallel to $[110]$, the simulation exhibits the broad peaks in the specific heat observed in experiments.^{61,62} It is likely that the $T = 1.1$ K specific heat feature corresponds to the $T = 1.1$ K feature found in polycrystalline samples of $\text{Dy}_2\text{Ti}_2\text{O}_7$.^{29,88}

VII. CONCLUSION

We have reviewed much of the early experimental and theoretical work on the static magnetic properties of spin ice. We have also clarified our principle point of view that long-range dipolar interactions are consistent with and responsible for the physics observed in spin ice materials based on Dy^{3+} and Ho^{3+} rare earth ions. Support for our perspective resides in the detailed Monte Carlo and mean-field calculations presented in this paper.

Monte Carlo simulations were performed on the dipolar spin ice model with the long-range dipole-dipole interactions treated via the Ewald method. Using a single spin flip Monte Carlo method, we were able to study the development of the spin ice manifold. We found that spins freeze out at temperatures $O(1\text{K})$ with a macroscopic degeneracy or residual Pauling entropy. We also found that single spin flip dynamics are not effective at equilibrating the system, thus making it impossible to determine the ordered state of spin ice by this technique.

Mean-field theory (Gaussian approximation) was applied to the same dipolar spin ice Hamiltonian with the dipolar interactions treated via the Ewald method in \mathbf{q} -space. There, we showed that an ordering wave vector may be selected and that a proper treatment of the long-range dipoles is crucial to achieving a consistent picture with the experiments. A key point is that the symmetry of self-screening is not exact for the dipolar Hamiltonian. In the end, we found a quasi-degenerate spectrum emerges with a commensurate critical mode ($\mathbf{q} = (0, 0, 2\pi/a)$) and a two-in two-out spin ice structure.

In order to find the ordered state of spin ice in a Monte Carlo simulation, we developed a non-local algorithm that employs loop moves (or updates) when inside the spin ice manifold. These loop moves represent the “nearly” zero energy collective dynamics that allow our model to sample the highly degenerate phase space of spin ice. Application of this method at temperatures within the spin ice manifold, i.e., $T \lesssim 1\text{K}$, leads to the selection of a single spin ice ground state configuration with $\mathbf{q} = (0, 0, 2\pi/a)$. The loop Monte Carlo and mean-field results agree. In addition, we find a first order transition to the ground state at $T_c \approx 180\text{ mK}$, which recovers all of the residual Pauling entropy of the spin ice manifold. Our physical understanding of spin ice is aided by the picture that any collective dynamics in real spin ice materials are inhibited by a freezing process as the system enters the temperature range where the ice-rules fulfilling manifold develops, i.e., $T_{\text{freeze}} \approx 0.4\text{ K}$ for $\text{Dy}_2\text{Ti}_2\text{O}_7$ and $T_{\text{freeze}} \approx 0.6\text{ K}$ for $\text{Ho}_2\text{Ti}_2\text{O}_7$ compared to $T_c \approx 180\text{ mK}$.

On the strength of the experimental evidence and the success of the dipolar spin ice model, we assert that both $\text{Ho}_2\text{Ti}_2\text{O}_7$ and $\text{Dy}_2\text{Ti}_2\text{O}_7$ are spin ice materials.

Finally, we have reflected on the application of a magnetic field to the spin ice materials as means of exploring the possible structures of the spin ice manifold and to further characterize the interactions present in these intriguing systems. We find excellent agreement between the dipolar spin ice model and many experimental studies to date. In addition, we find evidence for a low-temperature ordering transition to a $\mathbf{q} = X$ ground state for small magnetic fields parallel to the [110] crystal direction, that has not yet been observed. Some of the results presented here regarding the behavior of spin ice are intriguing. This argues for more theoretical, numerical and experimental work, to resolve all the perplexing issues at stake.

VIII. ACKNOWLEDGMENTS

We thank S. Bramwell, J. Gardner, H. Molavian, and A. del Maestro for useful discussions. We are grateful to A. Ramirez for making available his specific heat data. We also thank R. Higashinaka, H. Fukazawa and Y. Maeno for their ongoing and very fruitful collaboration. R.G.M. acknowledges support from the US Department of Energy grant# DOE DE-FG02-03ER-46048 for a portion of this work carried out at UCSB. M.G. acknowledges financial support from NSERC of Canada, the Canada Research Chair Program, Research Corporation, and the Province of Ontario.

APPENDIX A: EWALD

We give only a brief overview of the Ewald⁸⁹ technique as it applies to dipole-dipole interactions in Monte Carlo simulations and at the mean-field level. A more detailed

discussion of the method can be found in Refs. 73 and 90. The mean-field case as it applies to moments on the pyrochlore lattice is treated in depth in Ref. 52.

The dipole-dipole interaction is an infinite sum that falls off as the inverse cube of the separation distance between dipoles, $1/|\mathbf{R}_{ij}^{ab}|^3$. Hence it is a conditionally convergent series. The point of the Ewald method is to convert this slowly converging lattice sum into of two absolutely (rapidly) converging series, one in real space and the other in Fourier space. The general lattice sum for $\langle 111 \rangle$ Ising dipoles on the pyrochlore lattice is

$$\begin{aligned} \mathcal{A} &= \sum_{i,j} \sum_{a,b} \left(\frac{\hat{z}^a \cdot \hat{z}^b}{|\mathbf{R}_{ij}^{ab}|^3} - \frac{3(\hat{z}^a \cdot \mathbf{R}_{ij}^{ab})(\hat{z}^b \cdot \mathbf{R}_{ij}^{ab})}{|\mathbf{R}_{ij}^{ab}|^5} \right), \\ &= -(\hat{z}^a \cdot \nabla_{\mathbf{x}})(\hat{z}^b \cdot \nabla_{\mathbf{x}}) \left\{ \sum_{i,j} \sum_{a,b} \frac{1}{|\mathbf{R}_{ij}^{ab} - \mathbf{x}|} \right\}_{\mathbf{x}=0} \end{aligned} \quad (\text{A1})$$

where the spin variables σ_i^a have been dropped for notational convenience. The dipole sum excludes terms with $\mathbf{R}_{ij}^{ab} = 0$. Absolute convergence is forced on the sum inside the curly brackets of Eq. (A1) by use of a convergence factor. The form of this convergence factor differs depending on whether the dipolar sum is performed on N particles in real space (e.g., Monte Carlo and molecular dynamic simulations) or in the thermodynamic limit in momentum space (mean-field theory).

In our work, MC simulations are performed on 3 dimensional lattices of $L \times L \times L$ cubic cells of the pyrochlore lattice under periodic boundary conditions, thus there are $N = 16 \times L \times L \times L$ spins in the simulation cell. The separation of moments within a simulation cell is given by \mathbf{R}_{ij}^{ab} . The dipolar energy for any pair-wise interaction is calculated within the minimum image convention by summing replicas of the N -site simulation cell over spherical shells of radii $\mathbf{n} = L(n_x, n_y, n_z)$ (n_x, n_y, n_z are integers) with the inclusion of a spherical convergence factor $e^{-s|\mathbf{n}|^2}$. The effect of the convergence factor is removed from the final form of the Ewald equations by imposing the limit $s \rightarrow 0$. Therefore, the starting point for the Ewald method is the dipole-dipole pair interaction,

$$\mathcal{A}_{ij}^{ab}(s) = -(\hat{z}^a \cdot \nabla_{\mathbf{x}})(\hat{z}^b \cdot \nabla_{\mathbf{x}}) \left\{ \sum_{\mathbf{n}'} \frac{e^{-s|\mathbf{n}|^2}}{|\mathbf{n} + \mathbf{R}_{ij}^{ab} - \mathbf{x}|} \right\}_{\mathbf{x}=0}, \quad (\text{A2})$$

where $\sum_{\mathbf{n}'}$ means that $\mathbf{n} = 0$ is omitted whenever $\mathbf{R}_{ij}^{ab} = 0$. The point charge distribution, $1/|\mathbf{n} + \mathbf{R}_{ij}^{ab} - \mathbf{x}|$, is rewritten with the aid of the Γ -function identities,

$$\frac{1}{|\mathbf{x}|} = \frac{1}{\sqrt{\pi}} \int_0^\infty t^{-1/2} e^{-t|\mathbf{x}|^2} dt \quad (\text{A3})$$

$$= \frac{2}{\sqrt{\pi}} \int_0^\infty e^{-t^2|\mathbf{x}|^2} dt. \quad (\text{A4})$$

Using Eq. (A3), the pair-wise interaction becomes

$$\mathcal{A}_{ij}^{ab}(s) = -(\hat{z}^a \cdot \nabla_{\mathbf{x}})(\hat{z}^b \cdot \nabla_{\mathbf{x}}) \frac{1}{\sqrt{\pi}} \int_0^\infty dt \quad (\text{A5})$$

$$\times \left\{ \sum_{\mathbf{n}'} t^{-1/2} e^{-t|\mathbf{n} + \mathbf{R}_{ij}^{ab} - \mathbf{x}|^2 - s|\mathbf{n}|^2} \right\}_{\mathbf{x}=0},$$

and the remainder of the Ewald for calculation for \mathcal{A}_{ij}^{ab} follows arguments outlined in Ref. 90. The Ewald equations for a Monte Carlo simulation can also be found in Appendix A of Ref. 68. \mathcal{A}_{ij}^{ab} is calculated for each pairwise interaction, $\{(i, a), (j, b)\}$, in the simulation cell, but this need be done only once because the spins are fixed to the lattice points. These pair interactions are stored in a look-up table and used in the stochastic sampling and measurement procedures of a Monte Carlo simulation.

In mean-field theory, one considers the Fourier transform of the dipole-dipole interaction; therefore, the term $e^{-i\mathbf{q} \cdot \mathbf{R}_{ij}^{ab}}$ is included in Eq. (A1) and plays the role of a convergence factor as discussed in Ref. 90. With a convergence factor that is periodic as opposed to spherical in R , the derivation of the q -dependent Ewald equations follows the method of long waves introduced by Born and Huang, Ref. 73. As noted in Section III, the momentum dependent dipole-dipole interaction is determined between sub-lattice sites and is a component of $\mathcal{J}^{ab}(\mathbf{q})$, where $\mathcal{J}(\mathbf{q})$ is 4×4 matrix. Using Eq. (A4), we can write the dipolar contribution to $\mathcal{J}^{ab}(\mathbf{q})$ as

$$\begin{aligned} \mathcal{A}^{a,b}(\mathbf{q}) &= -(\hat{z}^a \cdot \nabla_{\mathbf{x}})(\hat{z}^b \cdot \nabla_{\mathbf{x}}) \frac{2}{\sqrt{\pi}} \int_0^\infty dt \quad (\text{A6}) \\ &\times \left\{ \sum_{(i,j)'} e^{-t^2|\mathbf{R}_{ij}^{ab} - \mathbf{x}|^2 - i\mathbf{q} \cdot \mathbf{R}_{ij}^{ab}} \right\}_{\mathbf{x}=0}, \end{aligned}$$

where $\sum_{(i,j)'}$ means the $i = j$ term is excluded when $a = b$. The remaining steps in the derivation of the \mathbf{q} -dependent Ewald equations can be found in Ref. 52. In this work, $\mathcal{A}^{a,b}(\mathbf{q})$ was determined in at each \mathbf{q} -point in the first zone of the (hhl) plane of the pyrochlore lattice and used in the formation of $\mathcal{J}(\mathbf{q})$ in Eq. (11). We note that the value of $\mathcal{A}^{a,b}(\mathbf{q})$ in the limit $\mathbf{q} \rightarrow 0$ depends on direction. The value of $\mathcal{A}^{a,b}(0)$ can be related to the demagnetization factor.^{91,92}

APPENDIX B: $\chi(\mathbf{q})$ FROM A HIGH TEMPERATURE SERIES EXPANSION

We demonstrate that the mean field description of the static susceptibility,⁴⁶ $\chi(\mathbf{q})$, can also be derived from a high temperature series expansion (HTSE) to lowest order in β . In our HTSE, where there is no reliance on a mean-field approximation, we show that the same functional dependence on the eigenvalues that leads to a minimum in the free energy also defines the maximum in the response function of the local magnetization, which we interpret as a transition to a long-range ordered state at the Gaussian level. We use the model for local $\langle 111 \rangle$ Ising spins on the pyrochlore lattice, Eq. (6), but the final results are applicable, with minor modifications for the

spin components, to a general Heisenberg Hamiltonian. The Ising $\langle 111 \rangle$ Hamiltonian is

$$H = -\frac{1}{2} \sum_{i,j} \sum_{a,b} \mathcal{J}^{ab}(i,j) \sigma_i^a \sigma_j^b \quad (\text{B1})$$

where $\sigma_i^a = \pm 1$ are Ising variables and $\mathcal{J}^{ab}(i,j)$ is given by Eq. (7).

The \mathbf{q} -dependent susceptibility is defined as the Fourier transform of the two-point correlation function,

$$\chi(\mathbf{q}) = \frac{\beta}{N_{\text{cell}}} \sum_{a,b} \sum_{i,j} (\hat{z}^a \cdot \hat{z}^b) \langle \sigma_i^a \cdot \sigma_j^b \rangle e^{i\mathbf{q} \cdot \mathbf{R}_{ij}^{ab}}, \quad (\text{B2})$$

where $\beta = 1/T$ with temperature in units of k_B . We note that at this point $\chi(\mathbf{q})$ is a 4×4 matrix for Ising spins on the pyrochlore lattice. A HTSE for $\langle \sigma_i^a \sigma_j^b \rangle$ is expressed most clearly as an expansion of cummulants,⁹³

$$\langle \sigma_i^a \sigma_j^b \rangle = \sum_{m=0}^{\infty} \frac{(-\beta)^m}{m!} \langle \sigma_i^a \sigma_j^b H^m \rangle_c. \quad (\text{B3})$$

On the left hand side of Eq. (B3), $\langle \dots \rangle$ represents a thermal average and is thus a trace over states at finite T . The cummulants, $\langle \dots \rangle_c$, are expressed as traces over the $T = 0$ states (i.e., $\langle \dots \rangle_o = \text{Tr}\{\dots\}/2^N$). For our purposes, we need consider only the first two terms in the expansion,

$$\langle \sigma_i^a \sigma_j^b \rangle \approx \langle \sigma_i^a \sigma_j^b \rangle_c - \beta \langle \sigma_i^a \sigma_j^b H \rangle_c.$$

In the case of Ising spins, a non-zero trace has an even number of spin variables at each site. The zeroth order cumulant is determined trivially,

$$\langle \sigma_i^a \sigma_j^b \rangle_c = \langle \sigma_i^a \sigma_j^b \rangle_o = \delta_{ij} \delta^{ab}.$$

The first order contribution involves two terms,

$$\langle \sigma_i^a \sigma_j^b H \rangle_c = \langle \sigma_i^a \sigma_j^b H \rangle_o - \langle \sigma_i^a \sigma_j^b \rangle_o \langle H \rangle_o,$$

but the second does not contribute because $\langle H \rangle_o \propto \langle \sigma_i^c \sigma_m^d \rangle_o = 0$. Therefore, one has

$$\begin{aligned} \langle \sigma_i^a \sigma_j^b H \rangle_o &= -\frac{1}{2} \sum_{lm} \sum_{cd} \mathcal{J}^{cd}(l,m) \langle \sigma_i^a \sigma_j^b \sigma_m^c \sigma_l^d \rangle_o \\ &= -\mathcal{J}^{ab}(i,j). \end{aligned}$$

The \mathbf{q} -dependent susceptibility in the high temperature limit reads,

$$\chi(\mathbf{q}) \approx \frac{\beta}{N_{\text{cell}}} \sum_{a,b} \sum_{i,j} (\hat{z}^a \cdot \hat{z}^b) (\delta_{ij} \delta^{ab} + \beta \mathcal{J}^{ab}(i,j)) e^{i\mathbf{q} \cdot \mathbf{R}_{ij}^{ab}}. \quad (\text{B4})$$

Performing the Fourier transform of $\mathcal{J}^{ab}(i,j)$, the inverse of Eq. (10), we obtain

$$\chi(\mathbf{q}) = \beta \sum_{a,b} (\hat{z}^a \cdot \hat{z}^b) (\delta^{ab} + \beta \mathcal{J}^{ab}(\mathbf{q})), \quad (\text{B5})$$

where $\mathcal{J}(-\mathbf{q}) = \mathcal{J}(\mathbf{q})$ for a symmetric interaction matrix. The spin-spin interaction matrix and thus the susceptibility are diagonalized via the normal mode transformation given by Eq. (13). The unitary matrix, $U(\mathbf{q})$, that diagonalizes $\mathcal{J}(\mathbf{q})$ contains the orthonormalized eigenvectors of $\mathcal{J}(\mathbf{q})$, i.e., $\sum_{\alpha} U^{a,\alpha}(\mathbf{q})U^{b,\alpha}(-\mathbf{q}) = \mathbf{I}$, where \mathbf{I} is the 4×4 unit matrix. We use this to rewrite the two terms in Eq. (B5),

$$\delta^{ab} = \sum_{\alpha} \sum_{a,b} U^{a,\alpha}(\mathbf{q})U^{b,\alpha}(-\mathbf{q}), \quad (\text{B6})$$

and

$$\mathcal{J}^{ab}(\mathbf{q}) = \sum_{\alpha} \lambda^{\alpha}(\mathbf{q})U^{a,\alpha}(\mathbf{q})U^{b,\alpha}(-\mathbf{q}). \quad (\text{B7})$$

The expression for $\chi(\mathbf{q})$ now becomes,

$$\chi(\mathbf{q}) = \beta \sum_{\alpha} \sum_{a,b} (\hat{z}^a \cdot \hat{z}^b)(1 + \beta\lambda^{\alpha}(\mathbf{q}))U^{a,\alpha}(\mathbf{q})U^{b,\alpha}(-\mathbf{q}). \quad (\text{B8})$$

In the high temperature limit, $\beta \rightarrow 0$, and $1 + \beta\lambda^{\alpha}(\mathbf{q}) \approx 1/(1 - \beta\lambda^{\alpha}(\mathbf{q}))$; therefore, the static, \mathbf{q} -dependent susceptibility now reads,

$$\begin{aligned} \chi(\mathbf{q}) &= \beta \sum_{\alpha} \sum_{a,b} \frac{(\hat{z}^a \cdot \hat{z}^b)U^{a,\alpha}(\mathbf{q})U^{b,\alpha}(-\mathbf{q})}{(1 - \beta\lambda^{\alpha}(\mathbf{q}))} \quad (\text{B9}) \\ &= \beta \sum_{\alpha} \frac{|\sum_a \hat{z}^a U^{a,\alpha}(\mathbf{q})|^2}{(1 - \beta\lambda^{\alpha}(\mathbf{q}))}. \end{aligned}$$

Hence, as T approaches the ordering temperature defined by Eq. (15), $T_c = \lambda^{\max}(\mathbf{q}_{\text{ord}})$, the susceptibility diverges and signals a transition to a long-range ordered state.

APPENDIX C: DEMAGNETIZATION EFFECTS

When doing finite temperature Monte Carlo simulations on magnetic materials in an applied magnetic field, the effect of the boundary of the simulation cell must be carefully considered. For systems of interest, the dipolar spin ice Hamiltonian is augmented with a field dependent term, Eq. (29). The inclusion of this term in our Monte Carlo simulations leads to subtle effects. In a microscopic Hamiltonian, the field \mathbf{h} referred to in Eq. (29) is the sample *internal* field, i.e., the magnetic field that directly couples to each magnetic dipole moment. However in real materials, bulk demagnetization effects alter the magnitude of the internal field in a complicated manner that depends on sample size, shape, alignment, and surrounding medium. In general, experimentalists define three separate quantities (the magnetic flux density \mathbf{B} , the magnetic field strength \mathbf{H} , and the magnetization \mathbf{M}) to account for these effects. In a macroscopic material, these quantities are related by

$$\mathbf{B} = \mu_0(\mathbf{H} + \mathbf{M}), \quad (\text{C1})$$

where \mathbf{B} is the independent quantity controlled in the experiment, but \mathbf{H} is the field strength that couples to the spins (through which the bulk susceptibility is defined). In order to benchmark an experiment to a theory such as ours, an attempt must be made to relate the *external* experimental (applied) \mathbf{B} controlled by external sources of current to the internal \mathbf{h} of our Hamiltonian. From an experimental side, this amounts to knowing the internal \mathbf{M} associated with the specific sample being measured. This \mathbf{M} is in general not easily deduced; although, for certain sample shapes (e.g., ellipsoids of revolution) it is at least uniform, and fairly accurate estimates can be made. The procedure of correcting for \mathbf{M} to obtain \mathbf{H} is called making a demagnetization correction.

Theoretically, demagnetization effects are incorporated into a Monte Carlo simulation by imposing certain boundary conditions on the microscopic Hamiltonian in question. As described earlier, we use the Ewald summation method to calculate the long-range dipolar interactions of our model. We follow the standard approach in which the pair wise interactions are evaluated by summing over periodic copies of the N site simulation cell until convergence is obtained,⁹⁰ effectively simulating the infinite range nature of the dipoles. A consequence of this technique is that the finite size nature of the simulation cell is suppressed. We are, therefore, faced with the question of how to interpret an “infinite boundary”. If one wishes to simulate materials with no net magnetic moment, or materials with no internal demagnetizing field, no correction due to sample boundary is needed, and the simple Ewald sum results may be used. This is equivalent to simulating a long thin “needle” of the bulk material. However, if one wishes to simulate a material in which the unit cell has a net magnetic moment or internal demagnetizing fields, then we must modify the Ewald sum to take into account the necessary boundary effects. This is especially important in our simulation because the long-range nature of the dipole-dipole interactions greatly accentuates these effects.

The approach described by de Leeuw *et al.*⁹⁰ is to include a *boundary term* in the Ewald sum of the form

$$\left(\frac{4\pi}{2\mu' + 1} \right) \frac{\mu_i \cdot \mu_j}{L^3} \quad (\text{C2})$$

where μ_i is the magnetic dipole moment of a spin, and L is the system linear dimension. Physically, the inclusion of this term corresponds to the consideration of a region external to the spherical Ewald boundary (see discussion in Ref. 90). This external region is a continuum with magnetic permeability constant ranging from $\mu' = 1$ to infinity. Because of the nature of our Ewald sum, the $\mu' = 1$ case will in effect simulate the bulk of a spherical sample surrounded by a vacuum. The $\mu' = \infty$ case corresponds to simulating a bulk sample which is needle-like and parallel to an applied \mathbf{B} , and hence contains no internal demagnetizing field.

In summary, to make a meaningful comparison between simulation and experiment within the dipolar spin

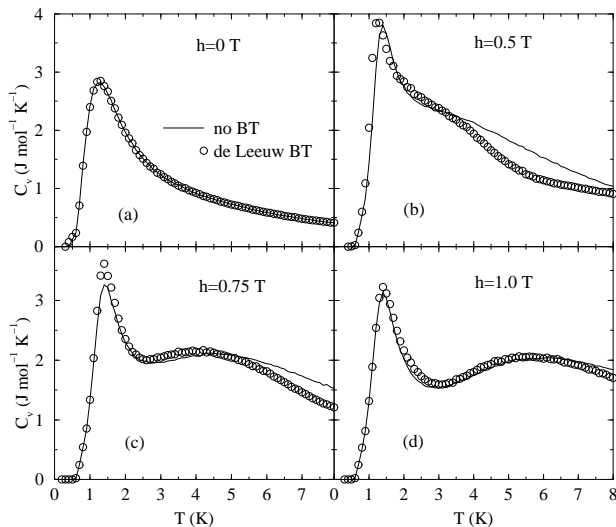


FIG. 29: Specific heat curves for $\text{Dy}_2\text{Ti}_2\text{O}_7$ in an applied field $\mathbf{h}/[110]$, in simulations without (line) and with (circles) the boundary term (BT) in the Ewald energy summation. These simulations employed single spin flip dynamics in the Monte Carlo. The significance of this data in the context of experimental measurements on $\text{Dy}_2\text{Ti}_2\text{O}_7$ is discussed in detail in Section VI.

ice model in an applied magnetic field, one of two scenarios must happen:

1. Simulations are performed using the regular Ewald summation method, and bulk demagnetization effects are accounted for by experimentalists.
2. Simulations are performed with the inclusion of a

boundary term Eq. (C2). Experimentalists are restricted to measurements on spherical samples to make quantitative comparisons. However, measurements on other sample shapes (with approximately constant internal fields) may allow some qualitative comparison.

The inclusion of the boundary term is a non-trivial matter in many simulations. For example, it will promote effects such as domain formation in simulations of global Ising ferromagnets. It is therefore always important to check ground state configurations of system where the term Eq. (C2) is absent against those where it has been included, in order not to miss any important secondary effects.

As a means of addressing some of these issues, we present some preliminary results on Monte Carlo simulations of the dipolar spin ice model. Fig. 29 shows specific heat curves for $\text{Dy}_2\text{Ti}_2\text{O}_7$ in an applied magnetic field, with and without the inclusion of the boundary term, Eq. (C2) with $\mu' = 1$. The results presented in Fig. 29 were performed using single spin flip dynamics on a system of size $L = 3$. As we see, the boundary term does not effect the $h = 0$ specific heat curve. This is consistent with the understanding that the boundary term is only necessary in Monte Carlo programs where the simulation cell has a net magnetic moment (which is not true in general for the spin ice manifold). For moderate fields, we see that the boundary term significantly alters the shape of the specific heat curve, as expected, since the simulation cell is acquiring a net magnetic moment. For very large fields, the boundary term begins to lose its effect, as the field term (Eq. (29)) becomes dominant in the Hamiltonian.

-
- ¹ G. Toulouse, *Commun. Phys.* **2**, 115 (1977).
 - ² J. Villain, *Z. Phys. B* **33**, 31 (1979).
 - ³ *Magnetic Systems with Competing interactions*, edited by H.T. Diep (World Scientific, Singapore, 1994).
 - ⁴ See Proceedings of Waterloo Conference on Highly Frustrated Magnetism: *Canadian Journal of Physics*, **79**, 1283-1596 (2001).
 - ⁵ A.P. Schiffer and A.P. Ramirez, *Comm. Cond. Mat. Phys.*, **18**, 21, (1996).
 - ⁶ J. E. Greedan, *J. Mater. Chem.* **11**, 37 (2001).
 - ⁷ R. Moessner, *Can. J. Phys.*, **79**, 1283 (2001).
 - ⁸ C.L. Henley, *Can. J. Phys.*, **79**, 1307 (2001).
 - ⁹ S.T. Bramwell and M.J.P. Gingras, *Science* **294**, 1405 (2001).
 - ¹⁰ R. Moessner and J. T. Chalker, *Phys. Rev. Lett.*, **80**, 2929 (1998); R. Moessner and J.T. Chalker, *Phys. Rev. B* **58**, 12049 (1998).
 - ¹¹ B. S. Shastry, cond-mat/0210230, unpublished.
 - ¹² C. Lhuillier and G. Misguich, cond-mat/0109146, unpublished.
 - ¹³ G. Misguich, D. Serban and V. Pasquier, cond-mat/0204428, unpublished.
 - ¹⁴ C. Lhuillier, P. Sindzingre, and J.-B. Fouet *Can. J. Phys.*, **79**, 1525 (2001).
 - ¹⁵ P. Sindzingre, J.-B. Fouet and C. Lhuillier, *Phys. Rev. B* **66**, 174424 (2002).
 - ¹⁶ R. Moessner and S. L. Sondhi, *Phys. Rev. Lett.* **86**, 1881 (2001); M. Hermele, M. P. A. Fisher, and L. Balents, cond-mat/0305401, unpublished.
 - ¹⁷ N. Büttgen, H. Kaps, W. Trinkl, A. Loidl, M. Klemm, and S. Horn, *Can. J. Phys.*, **79**, 1487 (2001).
 - ¹⁸ C. Lacroix, *Can. J. Phys.*, **79**, 1469 (2001).
 - ¹⁹ R. Ballou, *Can. J. Phys.*, **79**, 1475 (2001).
 - ²⁰ M. J. Harris, S. T. Bramwell, D. F. McMorrow, T. Zeiske, and K. W. Godfrey, *Phys. Rev. Lett.* **79**, 2554 (1997).
 - ²¹ S.T. Bramwell and M.J. Harris, *Phys. Condens. Matt.* **10**, L215 (1998).
 - ²² Anderson had already pointed out the analogy of the relationship between the Ising antiferromagnet model on the spinel lattice (which is the same magnetic lattice as the pyrochlore lattice of corner-sharing tetrahedra) with that of ice water. P. W. Anderson, *Phys. Rev.* **102** 1008 (1956).

- ²³ We write the nearest-neighbor ferromagnetic model $H = -J \sum_{\langle ia,jb \rangle} \mathbf{S}_i^a \cdot \mathbf{S}_j^b$, where $J > 0$ is ferromagnetic, i, j denote FCC lattice points, and a, b label the sublattice. For Ising spins that point along a local $\langle 111 \rangle$ direction we write $\mathbf{S}_i^a = \sigma_i^a \hat{z}^a$, with $\sigma_i^a = \pm 1$ and \hat{z}^a defining the local $\langle 111 \rangle$ axis on the a sublattice, so we have $H = (+J/3) \sum_{\langle ia,jb \rangle} \sigma_i^a \sigma_j^b$ since $\hat{z}^a \cdot \hat{z}^b = -1/3$ on the pyrochlore lattice. This is the Hamiltonian of a pyrochlore *antiferromagnet* with *global* (fictitious) \hat{z} quantization axis direction and with nearest-neighbor coupling constant $+J/3$. Hence, the local $\langle 111 \rangle$ Ising ferromagnet on the pyrochlore lattice maps onto the global Ising antiferromagnet on the same lattice, as studied by Anderson in Ref. 22. For antiferromagnetic exchange, $J < 0$, the same argument shows that there are two ground states related by a global spin reversal symmetry $\mathbf{S}_i \rightarrow -\mathbf{S}_i$ and which correspond to all spins in or all spins out on the tetrahedra unit cells and is therefore a simple and non-frustrated problem as pointed out in S. T. Bramwell, M. J. P. Gingras, J. N. Reimers, J. Appl. Phys. **75**, 5523 (1994).
- ²⁴ J. D. Bernal and R. H. Fowler, J. Chem. Phys. **1**, 515 (1933).
- ²⁵ L. Pauling, J. Am. Chem. Soc. **57**, 2680 (1935).
- ²⁶ L. Pauling, *The Nature of the Chemical Bond*, Cornell University Press, Ithaca, NY, pp.464-469 (1960).
- ²⁷ W. F. Giaque and M. F. Ashley, Phys. Rev. **43**, 81 (1933); W. F. Giaque and J. W. Stout, J. Am. Chem. Soc. **58**, 1144 (1936).
- ²⁸ S. Rosenkranz, A. P. Ramirez, A. Hayashi, R. J. Cava, R. Siddharthan, and B. S. Shastry, J. Appl. Phys., **87**, 5914 (2000).
- ²⁹ A. P. Ramirez, A. Hayashi, R. J. Cava, R. Siddharthan, and B. S. Shastry, Nature **399**, 333 (1999).
- ³⁰ M. Harris, Nature **399**, 311 (1999).
- ³¹ R. Siddharthan, B. S. Shastry, A. P. Ramirez, A. Hayashi, R. J. Cava, and S. Rosenkranz, Phys. Rev. Lett. **83**, 1854 (1999).
- ³² R. Siddharthan, B. S. Shastry, A. P. Ramirez, Phys. Rev. B **63**, 184412 (2001).
- ³³ S.T. Bramwell, M. J. Harris, B. C. den Hertog, M. J. P. Gingras, J. S. Gardner, D. F. McMorrow, A. R. Wildes, A. L. Cornelius, J. D. M. Champion, R. G. Melko, and T. Fennell, Phys. Rev. Lett. **87**, 047205 (2001).
- ³⁴ A.L. Cornelius and J.S. Gardner, Phys. Rev. B **64**, 060406 (2001).
- ³⁵ O. A. Petrenko, M. R. Lees, and G. Balakrishnan, Phys. Rev. B **68**, 012406 (2003).
- ³⁶ V. Bondah-Jagalu and S.T. Bramwell, Can. J. Phys., **79**, 1381 (2001).
- ³⁷ H. Kadowaki, Y. Ishii, K. Matsuhira, and Y. Hinatsu, Phys. Rev. B **65**, 144421 (2002).
- ³⁸ K. Matsuhira, Y. Hinatsu, K. Tenya, H. Amitsuka, and T. Sakakibara, J. Phys. Soc. Jpn. **71**, 1576 (2002).
- ³⁹ C. Bansal, H. Kawanaka, H. Bando, and Y. Nishihara, Phys. Rev. B **66**, 052406 (2002).
- ⁴⁰ K. Matsuhira, Y. Hinatsu, K. Tenya, T. Sakakibara, J. Phys.: Condens. Matter **12**, L649 (2000).
- ⁴¹ K. Matsuhira, Y. Hinatsu and T. Sakakibara, J. Phys.: Condens. Matter **13** L737-L746, (2001).
- ⁴² J. Snyder, J. S. Slusky, R. J. Cava and P. Schiffer, Nature, **413** 48 (2001); Phys. Rev. B **66**, 064432 (2002).
- ⁴³ G Ehlers, A L Cornelius, M Orendác, M Kajnaková, T Fennell, S T Bramwell and J S Gardner, J. Phys.: Condens. Matter **15**, L9 (2003).
- ⁴⁴ B.C. den Hertog and M.J.P. Gingras, Phys. Rev. Lett. **84**, 3430 (2000).
- ⁴⁵ A.B. Harris, C. Kallin and A.J. Berlinsky, Phys. Rev. B **45**, 2899 (1992).
- ⁴⁶ J. N. Reimers, A. J. Berlinsky and A.-C. Shi, Phys. Rev. B **43**, 865 (1991).
- ⁴⁷ However, we note that for the open pyrochlore lattice structure, one would naively expect further neighbor exchange coupling to be very small. See discussion in J.E. Greedan, N.P. Raju, A.S. Wills, C. Morin, S.M. Shaw, and J.N. Reimers, Chem. Materials **10**, 3058 (1998).
- ⁴⁸ M. Kanada, Y. Yasui, Y. Kondo, S. Iikubo, M. Ito, H. Harashina, M. Sato, H. Okumura, K. Kakurai, H. Kadowaki, J. Phys. Soc. Jpn. **71**, 313 (2002).
- ⁴⁹ M. J. Harris, S. T. Bramwell, P. C. W. Holdsworth and J. D. M. Champion, Phys. Rev. Lett. **81**, 4496 (1998).
- ⁵⁰ J. D. M. Champion, S. T. Bramwell, P. C. W. Holdsworth and M. J. Harris, Europhys. Lett., **57**, 93 (2002).
- ⁵¹ M. J. P. Gingras and B. C. den Hertog, Can. J. Phys., **79**, 1339 (2001).
- ⁵² M. Enjalran and M.J.P. Gingras, cond-mat/0307151, unpublished.
- ⁵³ One could argue that such an ordering transition is what is found in Refs. 31 and 32 for some arbitrary choice of the cut-off distance for the dipolar interactions. We disagree with such a perspective, and see the issue at hand as much more subtle than that. Firstly, we adopt the point of view that the problem of conventional magnetic dipolar interactions with non-truncated $1/r^3$ interactions is an a priori extremely well defined Hamiltonian for which the precise question of what type of long-range ordered state emerges being also a very well defined statistical mechanics problem. Only when such a minimal model Hamiltonian has been understood (on its own theoretical merit), and tested against experiments, and had it been found to fail to describe the experiments, would we see merit to attempt modifying the spin Hamiltonian.^{31,32} This, in light of the agreement reported so far between experiments^{33,44,60} and the simple model Hamiltonian, Eq. (2), with long-range dipole interactions would seem unnecessary. On a more quantitative basis, we view the approach of Refs. 31 and 32 as *a priori* uncontrolled and the numerical results reported therein of little relevance to the finite temperature thermodynamics of the real materials. Indeed, the temperature scale for ordering in such truncated problem is obviously quantitatively affected by the specific choice of the cut-off distance. While the ground state for some cut-off distance may correspond to the true ground state for non-truncated dipolar interactions,^{32,54,55} such a truncated Hamiltonian will in general be inaccurate in terms of the paramagnetic correlations,^{51,52} and, more dramatically, result in nonzero temperature ordering and/or freezing phenomena unrelated to the non-truncated dipolar interactions.⁵¹
- ⁵⁴ B.S. Shastry, private communication.
- ⁵⁵ R. Siddharthan, Ph.D. thesis, Indian Institute of Science, Bangalore, 2000.
- ⁵⁶ G. T. Barkema, M. E. J. Newman, Phys. Rev. E **57**, 1155 (1998)
- ⁵⁷ M. E. J. Newmann and G. T. Barkema, *Monte Carlo Methods in Statistical Physics*, Clarendon Press, Oxford (1999).
- ⁵⁸ R. G. Melko, B. C. den Hertog and M. J. P. Gingras, Phys.

- Rev. Lett. **87** 067203 (2001).
- ⁵⁹ R. G. Melko, *M.Sc. Thesis*, University of Waterloo (2001).
- ⁶⁰ H. Fukazawa, R. G. Melko, R. Higashinaka, Y. Maeno, and M. J. P. Gingras, Phys. Rev. B **65**, 054410 (2002).
- ⁶¹ R. Higashinaka, H. Fukazawa, and Y. Maeno, Phys. Rev. B **68**, 014415 (2003).
- ⁶² Z. Hiroi, K. Matsuhira, and M. Ogata, cond-mat/0306240, unpublished.
- ⁶³ A. S. Wills, R. Ballou, and C. Lacroix, cond-mat/0208303, unpublished.
- ⁶⁴ K. Matsuhira, Z. Hiroi, T. Tayama, S. Takagi and T. Sakakibara, J. Phys.: Condens. Matter **14**, L559 (2002); Z. Hiroi, K. Matsuhira, S. Takagi, T. Tayama, and T. Sakakibara, cond-mat/0211326, unpublished.
- ⁶⁵ S.T. Bramwell, M.J.P. Gingras and J.N. Reimers, J. Appl. Phys. **75**, 5523 (1994).
- ⁶⁶ R. Moessner, Phys. Rev. B **57**, R5587 (1998).
- ⁶⁷ J. S. Gardner, S. R. Dunsiger, B. D. Gaulin, M. J. P. Gingras, J. E. Greedan, R. F. Kiefl, M. D. Lumsden, W. A. MacFarlane, N. P. Raju, J. E. Sonier, I. Swainson, and Z. Tun, Phys. Rev. Lett. **82**, 1012 (1999).
- ⁶⁸ M. J. P. Gingras, B. C. den Hertog, M. Faucher, J. S. Gardner, S. R. Dunsiger, L. J. Chang, B. D. Gaulin, N. P. Raju, and J. E. Greedan, Phys. Rev. B **62**, 6496 (2000).
- ⁶⁹ J. S. Gardner, B. D. Gaulin, A. J. Berlinsky, P. Waldron, S. R. Dunsiger, N. P. Raju, and J. E. Greedan, Phys. Rev. B **64**, 224416 (2001).
- ⁷⁰ Y. Yasui, M. Kanda, M. Ito, H. Harashina, M. Sato, H. Okumura, K. Kakurai, and H. Kadowaki, J. Phys. Soc. Jpn. **71**, 599 (2002).
- ⁷¹ Y.-J. Kao, M. Enjalran and M.J.P. Gingras, cond-mat/0207270, unpublished.
- ⁷² I. Mirebeau, I. N. Goncharenko, P. Cadavez-Peres, S. T. Bramwell, M. J. P. Gingras, and J. S. Gardner, Nature **420**, 54 (2002).
- ⁷³ J. M. Ziman, *Principles of the Theory of Solids*, 2nd ed., Cambridge University Press, Cambridge, 1972; M. Born and Huang, *Dynamical Theory of Crystal Lattices*, Oxford (1968).
- ⁷⁴ P. J. Camp, J. C. Shelley, and G. N. Patey, Phys. Rev. Lett. **84**, 115 (2000); G. Ayton, M. J. P. Gingras, and G. N. Patey, Phys. Rev. Lett. **75**, 2360 (1995).
- ⁷⁵ B.C. den Hertog, M.J.P. Gingras, S.T. Bramwell, and M.J. Harris, cond-mat/9912220, unpublished.
- ⁷⁶ H. W. J. Blote, R. F. Wielinga, and W. J. Huiskamp, Physica (Amsterdam) **43**, 549 (1969).
- ⁷⁷ A. P. Ramirez and J. Jensen, J. Phys.: Condens. Matter **6**, L215 (1994).
- ⁷⁸ E. Bertin, P. Bonville, J.-P. Bouchaud, and J. A. Hodges, Eur. Phys. J. B **27**, 347 (2002).
- ⁷⁹ We note here as well that, compared to the results of Ref. 29, the specific heat measurements reported by Blöte *et al.*⁷⁶ on Dy₂Ti₂O₇ do not suffer this problem: the total specific heat of Dy₂Ti₂O₇ in Ref. 76 never falls below the expected $1/T^2$ paramagnetic nuclear specific heat contribution.
- ⁸⁰ T. Fennell, O. A. Petrenko, G. Balakrishnan, S. T. Bramwell, J. D. M. Champion, B. Fåk, M. J. Harris, D. McK. Paul, Appl. Phys. A **74**, S889 (2002).
- ⁸¹ A.B. Harris, O.G. Mouritsen, and A.J. Berlinsky, Can. J. Phys. **62**, 915 (1984).
- ⁸² J. D. Shore and J. P. Sethna, Phys. Rev. B **46**, 11376 (1992).
- ⁸³ K. Binder and D. W. Heermann, *Monte Carlo Simulation in Statistical Physics*, Third Edition, Springer, Germany, (1997).
- ⁸⁴ B. A. Berg and T. Neuhaus, Phys. Rev. Lett. **68**, 9, (1992).
- ⁸⁵ U. H. E. Hansmann and Y. Okamoto, Physica A **212**, 415 (1994).
- ⁸⁶ A. M. Ferrenberg and R. H. Swendsen, Phys. Rev. Lett. **61**, 2635 (1988).
- ⁸⁷ R. Moessner and S. L. Sondhi, cond-mat/0303210, unpublished.
- ⁸⁸ R. Higashinaka, H. Fukazawa, D. Yanagishima, and Y. Maeno, J. Phys. Chem. Solids **63**, 1043 (2002).
- ⁸⁹ P.P. Ewald, Ann. Physik **64**, 253 (1921).
- ⁹⁰ S. W. de Leeuw, J. W. Perram and E. R. Smith, Ann. Rev. Phys. Chem. **37**, 245 (1986).
- ⁹¹ M.H. Cohen and F. Keffer, Phys. Rev. **99**, 1128 (1955).
- ⁹² A. Aharony and M.E. Fisher, Phys. Rev. B **8**, 3323 (1973).
- ⁹³ C. Domb, in *Phase Transitions and Critical Phenomena*, Vol. 3, Eds. Domb and Green, Academic Press., London, (1974).